frontiers in Earth Science

ORIGINAL RESEARCH
published: 18 October 2019
doi: 10.3389/feart.2019.00266

Concentric Structures and Hydrothermal Venting in the Western Desert, Egypt

Adriano Mazzini[1], Matteo Lupi[2], Alessandra Sciarra[3,4], Mohamed Hammed[5], Susanne T. Schmidt[2] and Annette Suessenberger[2]*

[1] Centre for Earth Evolution and Dynamics (CEED), University of Oslo, Oslo, Norway, [2] Department of Earth Sciences, University of Geneva, Geneva, Switzerland, [3] Istituto Nazionale di Geofisica e Vulcanologia, Rome, Italy, [4] Consiglio Nazionale delle Ricerche – Istituto di Geologia Ambientale e Geoingegneria, Rome, Italy, [5] Department of Geology, Faculty of Science, Cairo University, Cairo, Egypt

Large-scale concentric structures are enigmatic geological features observed on the Earth surface and on other planetary bodies. Their formation has been attributed to several processes. Here we describe for the first time the results of mapping and characterization of ∼100 large concentric circular structures found in Early Cenomanian argillaceous strata of the Bahariya depression (Egyptian Western Desert). The geological processes that lead to the formation of these features have remained so far elusive. We investigate the concentric structures with a multidisciplinary approach combining field observations, statistical analysis, soil-flux gas measurements and laboratory analyses of rock samples. The whole depression is dissected by the ∼90 km long N60°E-striking dextral strike-slip Bahariya fault. Effusive lavas and shallow intrusions crop out in the down faulted blocks. The mapped circular structures increase in number approaching the fault zone. These features are up to 10 m high and 625 m wide, have a morphology similar in shape to impact craters with steeper external flanks and a gently dipping internal subsided zone. Halite-cemented brecciated sediments from different geological units have been sampled in the central part of the concentric circular structures implying a subsurface mechanism involved in their formation. Petrography analyses revealed also the presence of high- and low-temperature minerals (e.g., Ba-K-feldspars and ferroaluminoceladonite) suggesting former phases of hydrothermal circulation. Soil-gas flux profiles (CO_2 and CH_4) reveal a modest CO_2 increase when crossing the central part of the circular structures inferring enhanced permeability. Field and laboratory data are consistent with a scenario envisaging a diffused and vigorous hydrothermal venting. The proposed scenario includes multiple phases where several geological elements and processes interact. The Bahariya fault, which activity initiated during the Late Cretaceous, provided pathways for Miocene magma ascent toward the surface and for the development of a network of subsurface intrusions in the organic-rich sedimentary rocks of the Bahariya Formation. The interaction of the igneous intrusions with carbon-rich sedimentary deposits produced overpressured fluids, causing the formation of sparse hydrothermal vents at the surface. The elongation of the main axis of the vents

OPEN ACCESS

Edited by:
Alessandro Tibaldi, University of Milano-Bicocca, Italy

Reviewed by:
Craig Magee, University of Leeds, United Kingdom
Basem Ahmed Zoheir, Benha University, Egypt

****Correspondence:***
Adriano Mazzini
Adriano.mazzini@geo.uio.no

Specialty section:
This article was submitted to Structural Geology and Tectonics, a section of the journal Frontiers in Earth Science

Received: *29 May 2019*
Accepted: *26 September 2019*
Published: *18 October 2019*

Citation:
Mazzini A, Lupi M, Sciarra A, Hammed M, Schmidt ST and Suessenberger A (2019) Concentric Structures and Hydrothermal Venting in the Western Desert, Egypt. Front. Earth Sci. 7:266. doi: 10.3389/feart.2019.00266

and the deformed structures located within the strike-slip zone suggest that faulting controlled the emplacement and the final shape of some of the hydrothermal vents. We speculate that this system may represent a palaeo sediment-hosted hydrothermal system and could be related to the opening of the Red Sea.

Keywords: strike-slip faulting, igneous intrusions, hydrothermal venting, sediment-hosted hydrothermal system, Bahariya depression, Egypt

INTRODUCTION

Circular structures are common geological features in nature, not only on planet Earth but also on other solid planets and moons of our solar system. The mechanisms leading to the formation of these circular structures is often complex and elusive. These geological features often represent the surface expression of complex phenomena occurring at greater depths. An insightful interpretation of the mechanisms leading to their formation may shed light on deep-rooted dynamics and ultimately on surface sedimentary and erosional processes.

Such puzzling structures have been documented e.g., on Mars, Ceres, Europa and have been associated to cryovolcanism, karst dissolution, erosional processes of meteorite impact craters, dilational faulting, or magma rise-related (e.g., Fagents, 2003; Wyrick et al., 2004; Edgett, 2005; Levy et al., 2010; Sori et al., 2017). On Earth, circular structures may be associated with differential erosion on anticlines and synclines folds with small inter-limb angles (Grotzinger et al., 2007), complex igneous intrusions such as the Richat structure in Mauritania (Matton et al., 2005), salt withdrawal basins and salt/shale diapirs (Vendeville and Jackson, 1992). Similar morphologies are also found in pull-apart basins (McDonnell et al., 2007), impact craters (Melosh and Ivanov, 1999), breccia pipes and hydrothermal vent complexes resulting from the eruption of fluids from sedimentary units affected by either igneous intrusions or hydrothermal fluids migration (e.g., Jamtveit et al., 2004; Svensen et al., 2006, 2007). Additionally, maar-diatreme resulting from magma–water interactions (White and Ross, 2011), offshore pockmarks forming at focused gas seepage sites (e.g., Mazzini et al., 2017) and karst subsurface dissolutions (Lucia, 1995) produce sub-circular geological structures. Earthquakes may also trigger the formation of such structures as shown by the New Madrid seismic sequence occurring in 1811-12 (Tuttle, 2005) when liquefaction and blow out of sedimentary units occurred in the near-field. Finally, the surface eruptive expression of mud volcanoes may create circular structures (Mazzini and Etiope, 2017).

The absence of vegetation and the reduced anthropogenic activity make desert regions ideal settings to study the interaction between geomorphological and geological processes. Although Aeolian deposits may hinder the study of local-scale geomorphological structures, large-scale features may be recognized by satellite images (e.g., Parrot and Taud, 1992; Stewart, 2015). Using this approach, several studies were conducted in the Egyptian Western Desert (Barakat, 1994; Tewksbury et al., 2009, 2012, 2014). This region is located to the west of the Nile River extending to the border with Libya (inset **Figure 1**). A number of enigmatic circular geological structures has been documented at several localities in this area. This type of features have been described in the Gilf Kebir plateau, near the near Farafra Oasis (inset **Figure 1**) and are described in detail in the geological setting section (Sandford, 1935; Klitzsch et al., 1987; Barakat, 1994; Paillou et al., 2006; Tewksbury et al., 2014). To the north of Farafra Oasis lies the Bahariya Depression (BD) (**Figure 1**). This region has been the focus of intensive geological studies following the discovery of economic iron ore deposits and records of various geological and archeological sites (Issawi, 1972; Franks, 1982; Dominik, 1985; El Sisi et al., 2002; Khalifa et al., 2002, 2003). Here we report the finding of nearly 100 concentric circular structures (CS) scattered around a large scale strike-slip fault system crossing the depression.

The goal of this paper is to describe the CS found in the BD providing information on their geological setting in relation to faulting and volcanism, their spatial distribution, and the mineralogical characteristics of such intriguing structures. We test if the hypotheses suggested for the formation of the other circular structures documented worldwide and in the Western Desert are applicable also for the features observed in the BD. Finally, we propose a tentative scenario to explain the geological formation and evolution of the CS in the BD.

GEOLOGICAL SETTING

The Bahariya depression is located in the Egyptian Western Desert comprised between latitudes 27°48′N and 28°30′N and longitudes 28°35′E and 29°10′E (**Figure 1**). The largest width measured normal to the longer axis is about 42 km. The area was naturally eroded to a large oval shape with a major axis running southwest-northeast for approximately 90 km. The average depth of the BD from the general desert plateau level to the floor of the excavation is less than 100 m. The excavation of the BD was attributed to wind and paleokarst processes promoted by the paleo structural configuration (Said, 1962; El Aref et al., 1987). Natural hydrothermal springs in the region are known since Roman times (El Sisi et al., 2002). Hot fluids were still emitted from artesian springs in the late 1970's (Ministry of Public Works and Water Resources [MPWWR], 1998; Plyusnina et al., 2016) before agricultural development caused the deepening of the groundwater table. Today, hot fluids (up to 50°C) are found at shallow depths (i.e., 300–500 m) and extracted for thermal bathing and

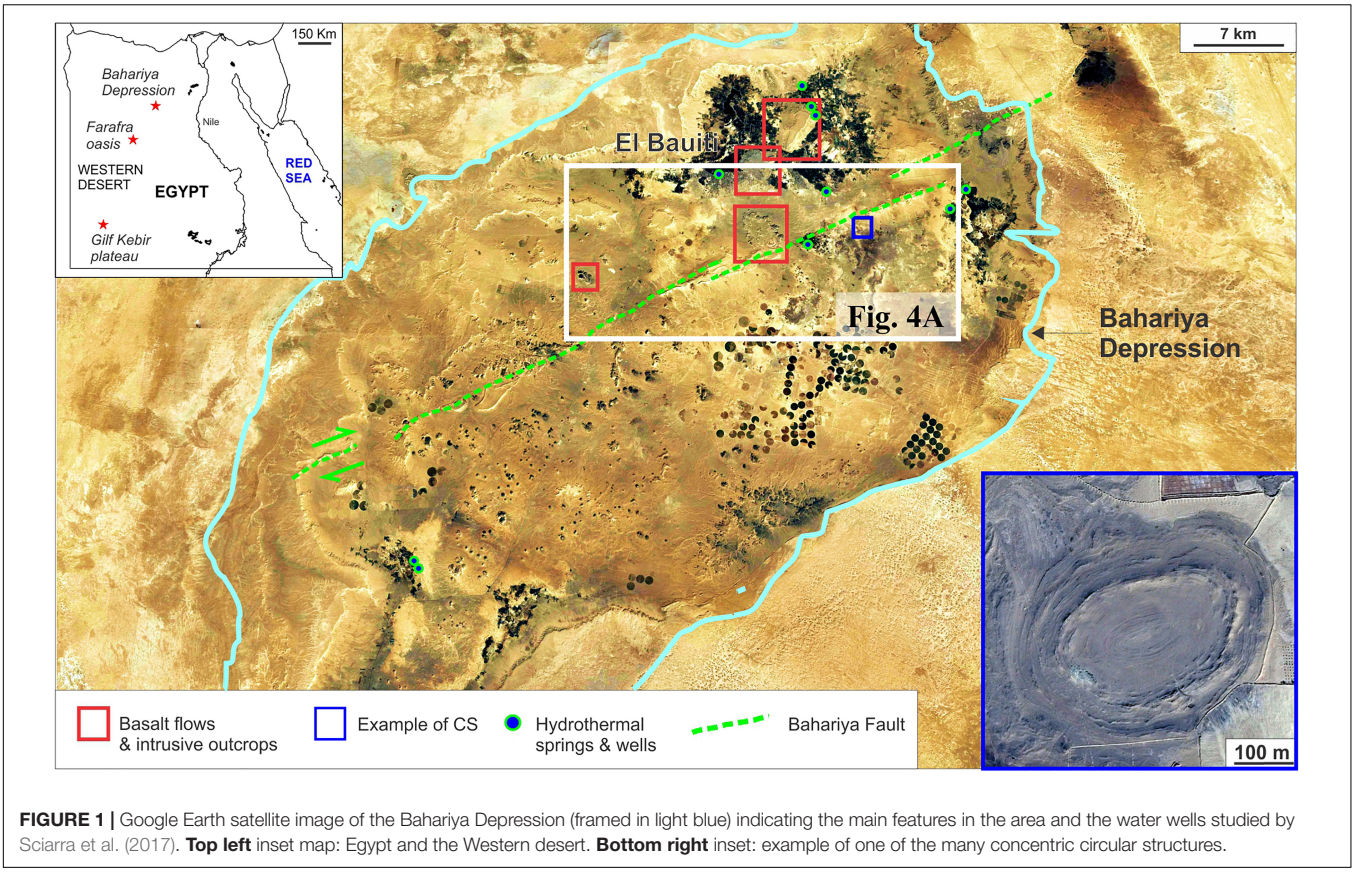

FIGURE 1 | Google Earth satellite image of the Bahariya Depression (framed in light blue) indicating the main features in the area and the water wells studied by Sciarra et al. (2017). **Top left** inset map: Egypt and the Western desert. **Bottom right** inset: example of one of the many concentric circular structures.

farming. Several of the modern wells are positioned at the same localities of ancient hydrothermal natural springs. Around these localities are present dozens of enigmatic CS whose origin remains so far unknown.

Similar circular structures have already been documented in other regions of the Western Desert and various mechanisms that may have led to their development are suggested. For example, the Gilf Kebir plateau (Barakat, 1994; Paillou et al., 2004; Paillou et al., 2006) features a high density of circular structures similar to the one showed in the panel of **Figure 1**. Initial observations of Klitzsch et al. (1987) associated these features with a few small Tertiary alkali-olivine basaltic outcrops in the north-western part of the region. Other analogous features (the Clayton craters) have been interpreted to be of volcanic origin (Clayton, 1933; Sandford, 1935). Paillou et al. (2004, 2006) used extracts of the SPOT 4 mosaic to report the presence of 1312 structures to the NE of the Gilf Kebir plateau. The circular features are distributed over an area of more than 40,000 km^2 with some of them being characterized by a diameter of about 2000 m. Originally it was postulated that such subcircular features could have been caused by meteoritic impacts (Paillou et al., 2004). A hydrothermal venting mechanisms was later proposed based on the fact that some of the structures are cross-cut by basaltic dikes and assuming that magmatism took place after the formation of such circular features (Paillou et al., 2006).

Further to the north, polygonal fault systems have been documented in the chalk of the Cretaceous Khoman Formation near Farafra Oasis. Here about 2000 isolated circular features (50–200 m in diameter) have been described as capped by an inward dipping resistant limestone layer. Such structures appear to be spatially associated with polygon boundaries and triple junctions displaying radial vertical veins (Tewksbury et al., 2014). The authors define these structures as basins and interpreted them to be the result of fault-controlled upwelling of fluids.

Stratigraphy

The BD is enclaved in a plateau of Eocene carbonates. The age of the exposed sedimentary rocks in the BD range from Cenomanian to Middle Eocene (Said, 1962, **Figure 2A**). Early Cenomanian clastic sediments crop out on the floor and on the lateral escarpments of the BD (Bahariya Formation, **Figure 2A**). According to Said (1990), the exposed Bahariya Formation has a maximum thickness of ∼200 m and could be divided into four main units consisting of sandstone and alternating shales with fining upward depositional sequences with essentially sub-horizontal dipping (**Figure 2B**). In the northernmost part of the BD, the upper unit is well-exposed. Here vertebrate and invertebrate fossils provide an Early Cenomanian age (Stromer, 1914). The depositional setting is characterized by a near-shore estuarine to subtidal and intertidal environment with intermittent subaerial exposure (Soliman and Khalifa, 1993; Catuneanu et al., 2006).

Within the BD, there are numerous inselbergs of Cenomanian units capped with (a) ferricrite crusts similar to those of the

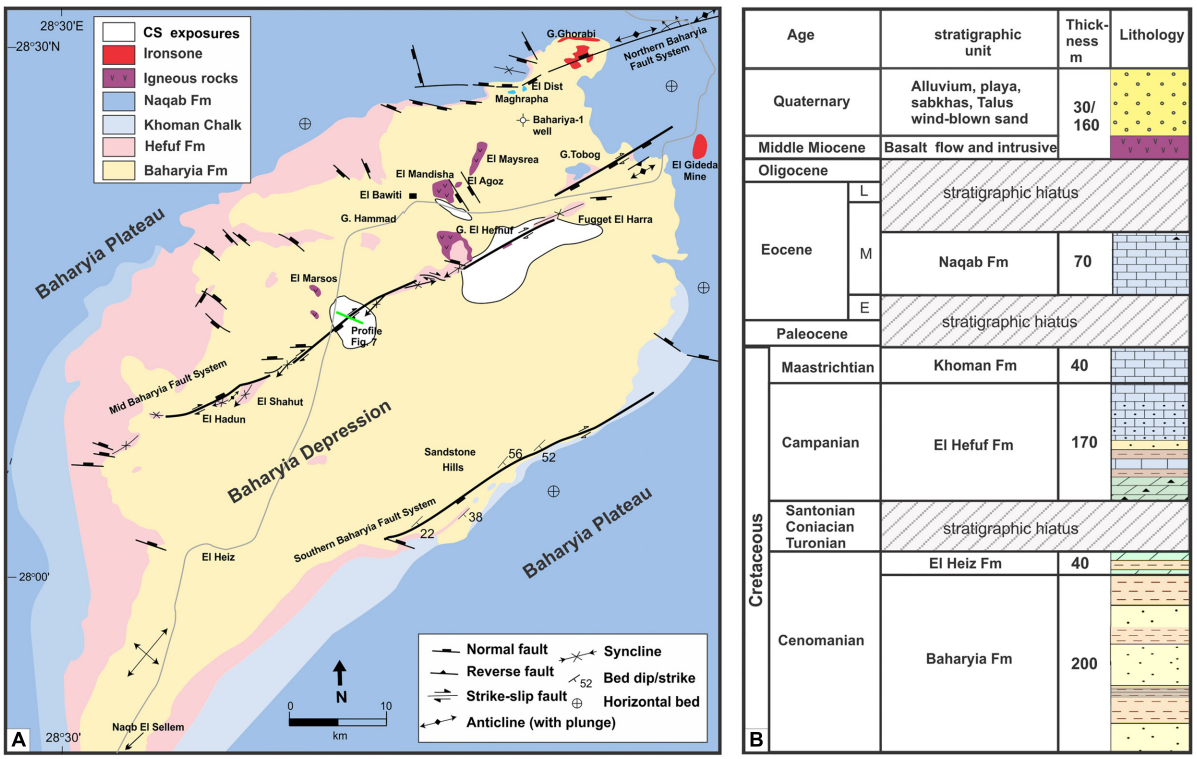

FIGURE 2 | (A) Geological map of the Bahariya Depression. **(B)** Generalized stratigraphic column with the main rock units, formations and stratigraphic hiatus inside and outside the Bahariya Depression.

Black Desert (El Aref et al., 1991; El Aref et al., 2017), (b) karstified Campanian and Eocene carbonates (El Heiz, El Hefuf, and Naqb Fms, and Knoman Chalks) such as those of Gebel Tobog, El Dist, El Maghrapha, Gebel Hammad, El Hefuf, and Fugget El Harra (**Figure 2A**) (El Aref et al., 2017), or (c) units of Oligo-Miocene basaltic intrusions and extruded magmatic volcanic units (**Figure 3**) (Meneisy, 1990; Bosworth et al., 2015; Khalaf and Hammed, 2016).

The Late Cenomanian El Heiz Fm. contains sandstones and siltstones rarely fossiliferous near the base, and dolostones at the top. The El Hefhuf Fm. (Campanian) is an unfossiliferous dolostone with sandstone intercalations in its middle part. The Lower to Middle Maastrichtian Khoman Chalk is a chalky limestones with a maximum thickness of 22 m. The surrounding plateau and few inselbergs within the BD are mainly capped by the Naqb Fm. The latter consist of Middle Eocene (Lower Lutetian) pinkish-yellow limestones and dolostones and is 35.5 m thick in the Northern part of the BD (Ismail et al., 1989).

An extensive replacement of the Middle Eocene Naqb Fm. carbonates by Fe and Mn oxides and quartz occurs near the major right-lateral strike-slip fault where carbonate units are partially or totally altered into cherty ironstone. The original fabrics and fossil contents of the host carbonates are still preserved and were replaced by iron (El Aref et al., 1999). The lower part of the exposed Bahariya Formation is characterized by the abundance of ferruginous sandstones altered by local weathering ultimately promoting the formation of prominent iron crusts (El Aref et al., 1999; Tanner and Khalifa, 2010; Afify, 2016). Based on field observations the timing of Fe-mineralization was dated as post-Middle Eocene (Nakhla, 1961; El Akkad and Issawi, 1963; Basta and Amer, 1969).

About 6000 ft (1890 m) of Paleozoic to Lower Cretaceous clastics units of shale and sandstones with Late Jurassic and Aptian intervals of carbonates were drilled by the Bahariya-1 exploratory borehole within the depression (Said, 1962). More precisely, the Paleozoic section intersected by the well is 1,024 m (about 3,350 ft) thick and consists of abundant Middle Cambrian shale beds in its lower unit (436 m thick) that lies with an unconformity on the Precambrian basement rocks. A 588-m-thick Late Carboniferous to Early Permian sandstone unit with some shale beds at the top overlies it with an unconformity (**Figure 4**, Moustafa et al., 2003).

Groundwater wells drilled in proximity of CS penetrate on average 700 m of Cenomanian clastics units of the Bahariya Formation (**Figure 2B**, Moustafa et al., 2003). Resistivity and gamma logs as well as the samples recovered from the borehole reveal a succession of sandstone and shales displaying a remarkable increase in organic content toward the bottom of the wells (Personal Comm. REGO Company, 2016).

Strike-Slip Faulting

Said (1962) described the whole BD as a Late Cretaceous eroded anticline, related to the NE- oriented folds of the compressional Syrian Arc system. The axis of this large anticline fold extends

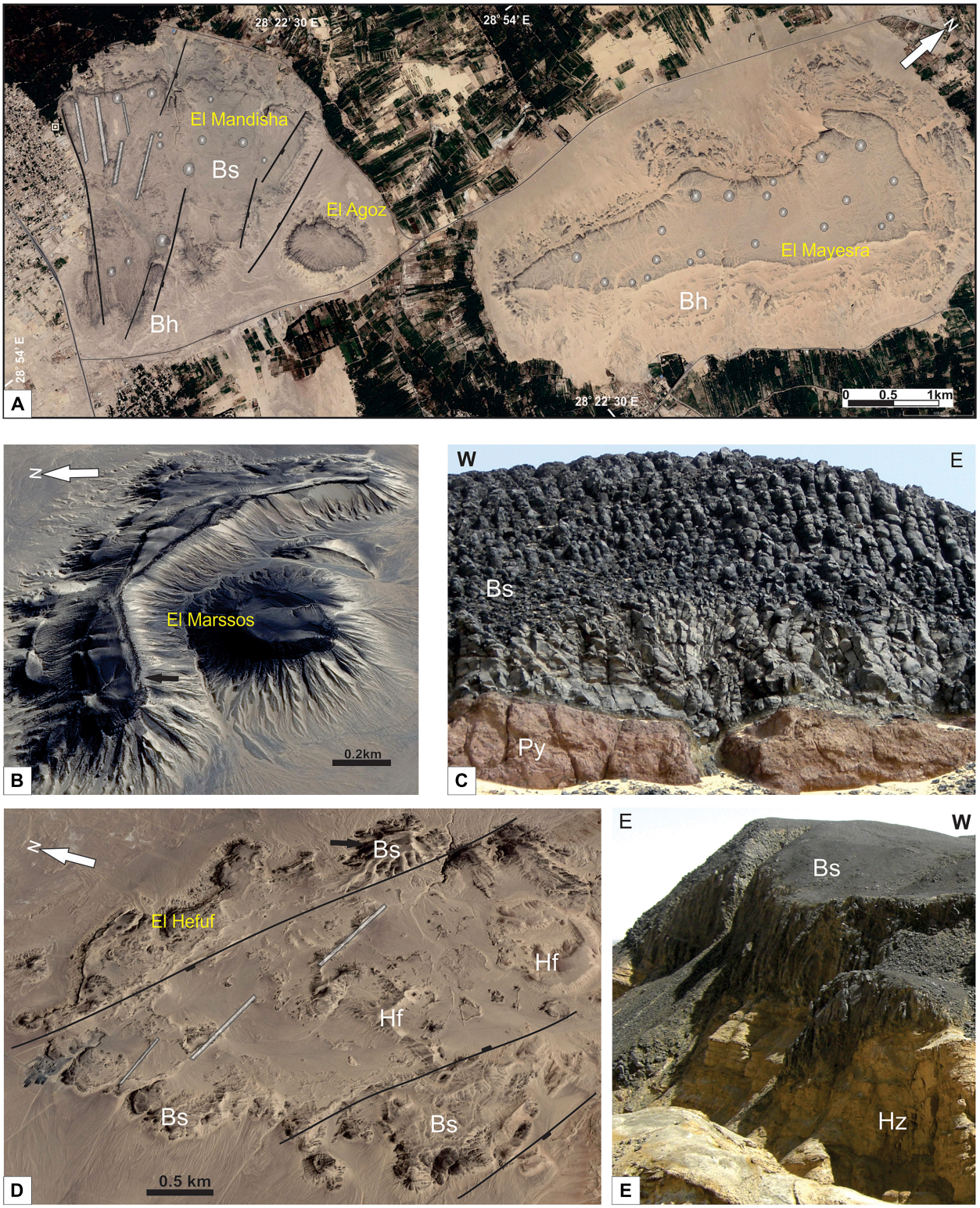

FIGURE 3 | Volcanic outcrops within the BD. **(A)** Google earth image of El Mandisha (left), El Agoz (center), and El Mayesra (right) volcanic flows with N60°W dikes as feeders (gray bars) and tumuli features (circles), note the N30°W normal faults dissecting the flows (black lines). **(B)** Google earth image showing the arched and plug liked outcrop of basaltic flow of El Marsos. **(C)** Volcanic conduit of basaltic flow within pyroclastic mound capped by columnar basalts at El Marsos outcrop. Additional details about this structure are provided in Khalaf and Hammed (2016). **(D)** Google Earth image shows basaltic occurrences at El Hefuf outcrop, Traced the NW- normal faults. **(E)** Basaltic flow of El Hefuf outcrop overlaying El Heiz Fm. Bs, basaltic flows; Bh, Bahariya Fm.; Py, Pyroclastic; Hf, El Hefuf Fm.; Hz, El Heiz Fm.

from Gebel Ghorabi in the north, toward the southwest direction at Naqb El Sellem, crossing the central isolated hills of the depression (Figure 6 in Said, 1962; Moustafa et al., 2003). However, additional subsurface studies indicate that the whole BD fold represents an overlap area between the extensional Jurassic to Early Late Cretaceous inherited northern and southern Baharyia Faults (El Nagar, 2012). A distinct Late Cretaceous right-lateral strike-slip deformation zone of the Mid Bahariya fault dissects the BD; this systems were occasionally reactivated during Late Eocene (right-lateral strike-slip) and Middle to Late Miocene (NE-directed extension) (Sehim, 1993; Moustafa et al., 2003). The authors highlight that these tectonic events are well expressed with three main E-NE-oriented fault systems (Northern, Mid- and Southern Bahariya fault systems) articulated across the BD (**Figure 2A**). Among the most prominent tectonic features dissecting the whole area, a series of anticlines and synclines are arranged in an echelon pattern along ENE-dextral wrench fault segments with reversal dip polarities of the Mid Bahariya fault system (**Figure 2A**). Many of the well-known structural assemblages associated with right-lateral simple shear strike-slip fault are recognized along the Mid Bahariya fault. These structures are particularly evident in the central north-eastern part of the BD where Gebel El Hefhuf, Fugget El Haara, and Gebel Tobog crop out (Moustafa et al., 2003; Sehim, 1993). All outcrops consist of highly deformed and tightly folded karstified Campanian strata which are overlain by gently folded Eocene carbonates at the top of Gebel Tobog (**Figure 2A**). The associated compressional and extensional structures are highlighted by the NE- reverse fault at the north-eastern escarpment and normal WNW-trending faults at El Mandisha and El Agoz areas (**Figure 2A**). Field evidences point out the kinematic evolution of the fault system (Sehim, 1993; Moustafa et al., 2003). The Late Cretaceous Maastrichtian (post-Campanian) faulting event can be constrained with geological methods. In fact, it is possible to observe the folding and dislocation of the Campanian strata (El Hefuf Fm.) along a ENE-striking right-lateral fault. The NE-striking reverse faults dislocate the Cenomanian strata in the El Haara area and it is also possible to recognize the NE-verging folding of the Cenomanian strata with steep dipping (Moustafa et al., 2003 and references therein). The Middle to Late Eocene faulting event is inferred by the re-folding of the El Hefuf Fm., the folding and dislocation of the Early Middle Eocene Naqb Fm., together with folding along the right-lateral fault segments. Finally, the dislocation of ironstone beds at Gebel Ghorabi and El Geidida Mine localities, and the W60–65°NW to NW extensional faulting associated with the right-lateral shears also help to constrain the age of the Middle to Late Eocene faulting event. This is also highlighted by the N30°W-striking extensional faults affecting the basaltic outcrops at El Mandisha and El Hefuf (**Figure 3A**).

Although the post-late -Eocene activity of the Mid Bahariya fault cannot be stratigraphically constrained in the Miocene-Quaternary sedimentary rocks (**Figures 2A,B**), frequent and later activities still could be proven by (i) the Oligocene N60°W doleritic dikes intruded along inherited faults at El Mandisha (Medani, 1995), (ii) Late Miocene N30°W normal faulting crossing the Oligo-Miocene volcanics, and (iii) recent earthquake record followed by reactivation of the Late Cretaceous dextral strike-slip fault to the north of the study area (Ezzelarab et al., 2018).

Volcanism and Shallow Intrusions

Remnant fields of effusive basaltic deposits and shallow intrusions are well preserved and exposed within the footwall block of the Mid Bahariya fault and form the hills (also called Gabal) of El Mandisha, El Mayesra, El Agoz, El Marssos, and El Hefuf (**Figure 2A**) (Khalaf and Hammed, 2016). These occurrences are mainly represented by basaltic units enriched in olivine and may change to dolerite with holocrystalline medium-grained groundmass in the intrusive varieties (El Qaluabi, 1974; Medani, 1995).

The basaltic lava flows at El Mandisha (**Figure 3A**) have a thickness of 10 m and thin down to 4 m moving northwards away from the Mid Baharyia Fault. The lava flows (Bs) can be subdivided into an upper fresh unit with spectacular columnar joints and a lower moderately weathered unit. The latter has intensive fracturing and a continuous sharp contact with the underlying Cenomanian rocks. Medani (1995) described a set of N60°W- trending doleritic dikes as a feeder of the basaltic flows which are dissected with N30°W normal faults distinguished with brecciated basaltic zones and rotation of the adjacent sedimentary rocks. To the east, El Agoz hill (∼400 m^2) forms an isolated exposure (**Figure 3A**) separated from El Mandisha by a N30°W-oriented normal fault that cuts through the basaltic flow and the underlying Bahariya Formation (Bh). The basaltic flows consist of vertical and horizontal tier of the rounded columnar joints particularly in the lower part of the basaltic flow (El Qaluabi, 1974; Khalaf et al., 2018). Further to the northeast, El Mayesra basaltic flows occur as an isolated NE-elongated sub-triangular outcrop (∼4 km long and 0.8 km wide, **Figure 3A**). According to Tosson (1964), these fissure eruption basalts occurred at the floor of the Bahariya depression.

El Marssos hill has a positive and plug-like shape reaching a thickness of more than 170 m above the base of the depression (**Figure 3B**). The basaltic flow has a distinct columnar structure resting on a ∼2 m thick pyroclastic mound of scoria lapilli, blocks, and bombs with mainly sub-millimeter vesicles exhibiting cauliflower structure (**Figure 3C**) (Khalaf et al., 2018). Both pyroclastics (Py) and flow (Bs) are overlying the sandstones and shales of the Bahariya Fm.

El Hefuf hill is aligned along the central segment of the Mid Bahariya fault. The exposure of the mafic rocks covers an area subelliptical in shape (7.4 km^2) elongated toward the NW, reaching the maximum thickness on the outer margin (**Figure 3D**). The hill consists of two basaltic sheets (sills) with well-developed colonnade overlying the cross-bedded sandstones and clastics of El Heiz and Bahariya Fms. and partially concordantly overlain by the sedimentary deposits of El Hefuf Fm. (El Akkad and Issawi, 1963; Medani, 1995). Toward the east, the N60°W doleritic dikes reach a thickness up to 3 m and dissect the Campanian rocks of El Hefuf Fm (Hf). Basaltic flows are observed in the central and eastern side of the area flooding the substratum of the Cenomanian clastics (El Heiz Fm., Hz; **Figure 3E**).

In the BD region, the volcanism has been initially dated (K-Ar) as Early to Middle Miocene, at about 20–15 Ma (Meneisy and El Kalioubi, 1975) and further Ar/Ar dating provided Oligocene-Miocene ages ranging between 20.8 and 25 Ma (Bosworth et al., 2015). However, the younger basaltic dikes and older pyroclastics beneath the lava flows were not included within the dated samples.

MATERIALS AND METHODS

Field Observations

In September 2015, a geological field survey was conducted in the BD to understand the interplay between strike-slip faulting, extrusive volcanism, and CS. The latter were targeted for detailed investigations to observe geometries and lateral discontinuities of the sedimentary layers. Shallow trenches were dug in the central area where rock samples were collected for petrographic analyses. Field observations of the basaltic rocks and fault zones were collected in order to constrain the emplacement of the basalts and the formation of the CS based on stratigraphic evidence.

Statistical Analyses

The position of the largest visible CS was mapped based on 2015 Google Earth satellite images and field observations. The size and distribution of each CS were uploaded and digitally treated using ArcMap (ArcGIS®) software. The digitalized database allowed extracting information such as the width of the CS, and their distance from the Mid Bahariya strike-slip fault system along a profile orthogonal to fault strike. We also calculated the direction of the longest axis of the CS. This dataset was used to elaborate statistical analyses and correlations. Different geospatial analysis techniques were applied to evaluate the basic characteristics of the raw data and their statistical distribution (Reimann and Filzmoser, 2000). In particular, plots of the frequency of occurrence of different events (e.g., diameter, perimeter, area and fault distance from the CS center) were designed. A circular histogram plot which displays directional data and the frequency of each class (Rose diagram) was used to display the main orientation of CS. Scatter graphs to plot points that show the relationship between two selected sets of data were also applied.

Geochemical Measurements

A 2.7 km long geochemical profile, including soil-gas measurements (He, Ne, H_2, CO_2, and CH_4), ^{222}Rn and ^{220}Rn activities, CO_2 and CH_4 flux records, was performed along a lineament intersecting almost perpendicularly the Mid Bahariya strike-slip fault (**Figure 2A**). The ^{222}Rn and ^{220}Rn activities were measured at 12 stations along the profile. The measurements were completed by inserting in the sand a 2 cm wide stainless steel probe connected with a silicon tube directly to a radon detector (RAD7, Durridge Co.) equipped with a solid-state alpha spectrometer. The probe was inserted at a depth of ∼80 cm in order to reduce the influence of atmospheric contamination (Hinkle, 1994). At these sites, gas samples were also collected from the probe using a plastic syringe and transferred into pre-evacuated vials. These containers were analyzed in the Fluid Geochemistry Laboratory at INGV Rome using a MicroGC Agilent 4900CP equipped with two Thermal Conductivity Detectors. 56 stations (spacing every 50 m) were completed along the profile to quantify CO_2 and CH_4 fluxes. The measurements were done by a speed-portable "closed dynamic" accumulation chamber "time zero" method (e.g., Cardellini et al., 2003). We used a West System^{TM} instrument equipped with two infrared spectrophotometer detectors. The CO_2 detector is a LICOR–LI820, which is accurate from 0 to 26400 g/m^2 day. This detector is a double beam infrared CO_2 sensor compensated for atmospheric temperature and pressure. Accuracy of the concentration reading is 2% and repeatability is ±5 ppm. The CH_4 flux meter is TDLAS (Tunable Diode Laser Absorption Spectroscopy) with multipass cell (West System assembled CH_4 sensor) with 10000 ppmv full-scale value that allows the measurement of flux in the range from 8 up to 24000 mg/m^2 day. The accuracy of the concentration reading is 0.1 ppmv, lower detection limit 0.1 ppmv. The data are transmitted via Bluetooth communication to a palmtop computer. The recorded concentrations measured over time, with other parameters such as volume and surface of the accumulation chamber, allow calculating the exhalation flux from soil (e.g., Hutchinson et al., 2000).

Petrography

A petrography study was conducted on the collected samples with SEM, electron microprobe and optical microscopes using a Hitachi SU5000 FE-SEM – Schottky FEG- and a Cameca SX100 with 5 WDS spectrometers (University of Oslo) and a JEOL JSM7001 F (University of Geneva). The images helped to characterize the various mineral generations and to provide a semi-quantitative chemical composition (EDS mode).

XRD analyses were performed on a Panalytical-Empyrean X-ray diffractometer (University of Geneva) using the gently crushed whole-rock powder method. The analyses were performed in continuous scan mode using Bragg-Brentano geometry, a step size of 0.013°2Θ and a scan rate of 0.55°/min in the range from 4 to 70° (45 kV, 40 mA, CuKα). The detection limit for qualitative mineral identification is around 5 wt%. The mineral determination was performed using the software HighScore Plus 3.0e.

RESULTS

Concentric Circular Structures and Statistical Analyses

A total of 94 large concentric structures (**Figures 4A–D**) were mapped in the well-exposed lower member of the Cenomanian Bahariya Formation. The shape of these structures varies from circular or subcircular (∼30%) (**Figure 4B**) with elongation along a preferential axis. Some of the CS are merged (**Figure 4C**), fewer have a sharply dissected shape if located at the intersection with the fault damage zones (**Figure 4D**).

Statistical analyses (**Table 1**) reveal that CS diameters range between 33 to 625 m and the 50% of the observations range between 96 and 217 m (lower and upper quartile

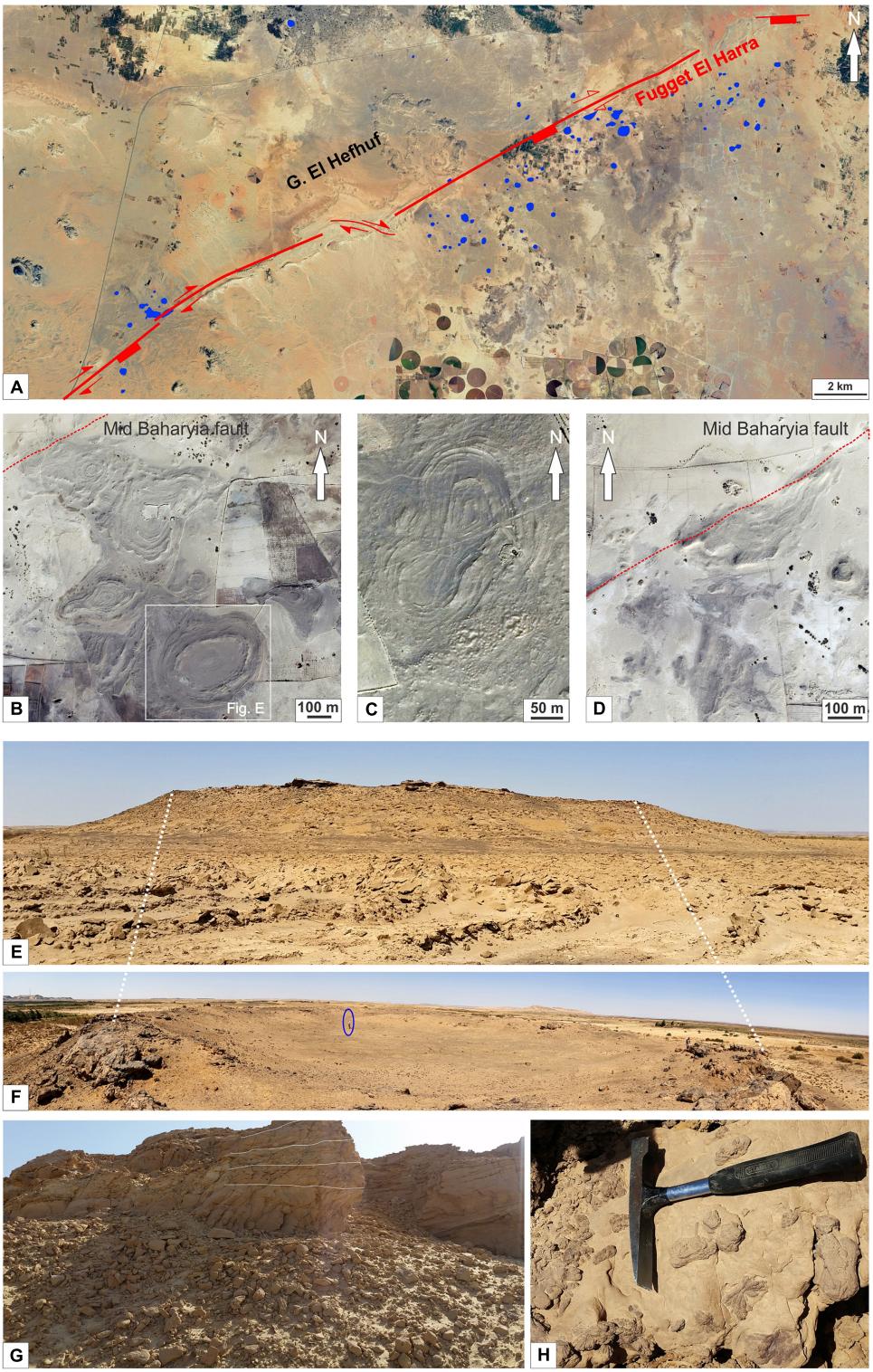

FIGURE 4 | Circular concentric structures in the Bahariya Depression. **(A)** Satellite image of the Bahariya Depression with CS mapped (framed in blue). Their concentration increases approaching the Bahariya fault (traced with red line) and is higher in the southern part of it. **(B–D)** Satellite image examples of CS fields. Note the internal ring pattern; the central part of these structures may occasionally be filled with sandy sediments. **(B)** Subcircular CS with increased deformation (from bottom to top) approaching the fault zone (indicated with red line). **(C)** Twinned and deformed CS. **(D)** Sharp cut of CS at the intersection with the fault (indicated with red line). **(E,F)** Field images of CS. Seen from aside **(E)** are visible the steeper external flanks while the internal structure **(F)** consist of a basin-like depression (man for scale). **(G)** Detail of one of the external flanks showing the layered sedimentary host rocks; **(H)** detail of one of the Ba-cemented sandstone beds with numerous desert roses on the surface.

TABLE 1 | Summary of the statistical analyses of main measured variables of CS in the studied area.

	Valid N	Mean	Geometric Mean	Median	Minimum–Maximum	LQ	UQ	Std. Dev.	CV	Sk	IQR
Perimeter (m)	94	532	446	456	103–1962	303	682	330	62	1.5	379
Area (m^2)	94	24448	13799	15386	787–163466	6704	32693	28133	115	2.6	25989
Diameter (m)	94	169	142	145	33–625	96	217	105	62	1.5	121
Fault distance (m)	94	1191	775	891	3–8195	445	1513	1192	100	3.0	1068

LQ, lower quartile; UQ, upper quartile; Std. Dev., standard deviation; Sk, skewness; CV, coefficient of variation; IQR, interquartile range.

respectively).The histogram of **Figure 5A** shows a log normal distribution that is also highlighted by the similarity between the median (145 m) and the geometric mean (142 m). The CS elevation from the external topography ranges from a few meters up to ∼10 m. The rose diagram **Figure 5B** shows that the axis of the elongated structures show a large variety of azimuths spanning from N19°E to N149°E. The most prominent group of elongated CS strikes with a direction around N40°E, which is subparallel to the direction of the Bahariya fault. A qualitative observation of satellite images seems to indicate that the CS distribution is higher in proximity of the Mid Bahariya fault. The statistical analysis confirms that most of the CS are clustered within 1000 m distance from the Mid Bahariya fault (**Figure 5C**). The plotted data show that the highest populations of occurrence are between 400–600 and 800–1000 m indicating a correlation between the development of the CS and the fault (**Figure 5C**). Statistical analyses of perimeter and distance from the fault in function of the CS area suggests that both variables are not stationary in the region, and that there are trends in the spatial distribution of data values (**Figures 5D,E**). Four classes of perimeter distribution can be identified using these parameters (**Figures 5D–F**). The CS are more abundant near the fault zone, and the highest amount occurs in the southern side of the fault (64%, **Figure 5D**). Fewer CS occur in the northern side and are located nearby outcrops of basalts. Some of the CS are deformed (in agreement with the kinematic of the Mid Bahariya Fault) and few are cut and displaced by the fault. This may suggests a localized shearing during the formation of the structure.

A cross section of the CS shows a saucer shape with steeper external flanks and a gently dipping internal morphology forming a smooth basin shape (**Figures 4E,F**). Both the external flanks and the internal structure of the CS consist of alternating sandstone and thinner shale beds of the lower Bahariya Formation (**Figures 4G,H**). The internal depressions of the CS display numerous concentric rings (**Figure 6A**). These rings are made of the same lithologies that are present in the surrounding areas (i.e., sandstones and shale). The circular shape is highlighted by the black interlayers of iron oxide separating the sandy beds. The dip of these beds (10° max, 5–8° on average) points inwards to the center of the structure. The central zone was targeted for detailed investigations. Here no obvious surface ring structures are visible possibly due to the deposition of Aeolian sediments. Up to at least 1 m depth are present halite-cemented clasts of brecciated shale and sandstone mixed with finer-grained sediments (**Figures 6B,C**).

Geochemical Profiles and Circulation of Fluids

The geochemical profile carried out across the Mid Bahariya fault lineament (**Figure 7**) revealed relatively modest values for the measured ^{222}Rn (between 62 and 1180 Bq/m^3), CO_2 (between 462 and 764 ppmv), H_2 (between 0.87 and 6.83 ppmv), ϕCO_2 (between 0.6 and 51 g/m^2day), ϕCH_4 (between 3 and 275 mg/m^2day). Some indications of focused degassing can be observed in the portions of the profile characterized by more obvious surface deformations. These deformations occur throughout a wide region around the main trace of the Mid Bahariya fault where additional secondary structures (extensional, compressional, shears) are associated with the master fault. Higher soil degassing values are recorded within a ∼500 m region around the faulted zone with an observed increase of the gaseous species (**Figures 7B,E**) and a decreasing of $^{220}Rn/^{222}Rn$ ratio (**Figure 7B**). The highest radon peak (1180 Bq/m^3) was measured at about 1.25 km from the beginning of the profile, near a CS. CO_2 and CH_4 soil-gas flux measurement profiles were completed across the CS. Results reveal a slightly higher concentration of CO_2 approaching the center with no significant CH_4 flux variations across the structures.

Petrography: Microscopic, XRD and SEM Studies

Petrography analyses of samples collected from the central part of the CS have been conducted (e.g., **Figures 6B–D**). Halite represents the main cementing phase for the larger clasts of brecciated units of sandstone and shale. Distinct subvertical conduits with significant amount of green and reddish-brown minerals are visible (**Figure 6D**).

Polarized microscopy observations and XRD determinations of the rock samples (**Figures 6G,H**) point out the presence of quartz, microcline (**Figure 8A**), rutile (**Figure 8B**), zircon (**Figure 8C**), and phengite as main components of the sandstone mineral assemblage, and K-feldspar, ferroaluminoceladonite, Ba-K-feldspar, sanidine, halite as authigenic minerals (**Figures 6E–H**). Ferroaluminoceladonite is responsible for the green color and Fe-oxide/hydroxide for the brown color of some specimens.

Detailed SEM investigations allowed determining at least three generations of K-feldspar growth. A first generation (GI) of an anhedral zoned Ba-rich orthoclase (**Figures 8D,E,H,K**), rimmed by a second generation (GII) of K-feldspar (**Figures 8D,E,H**). A third K-feldspar phase (GIII) is present as small euhedral crystals growing into open space (**Figures 8G,J**). The Ba-content

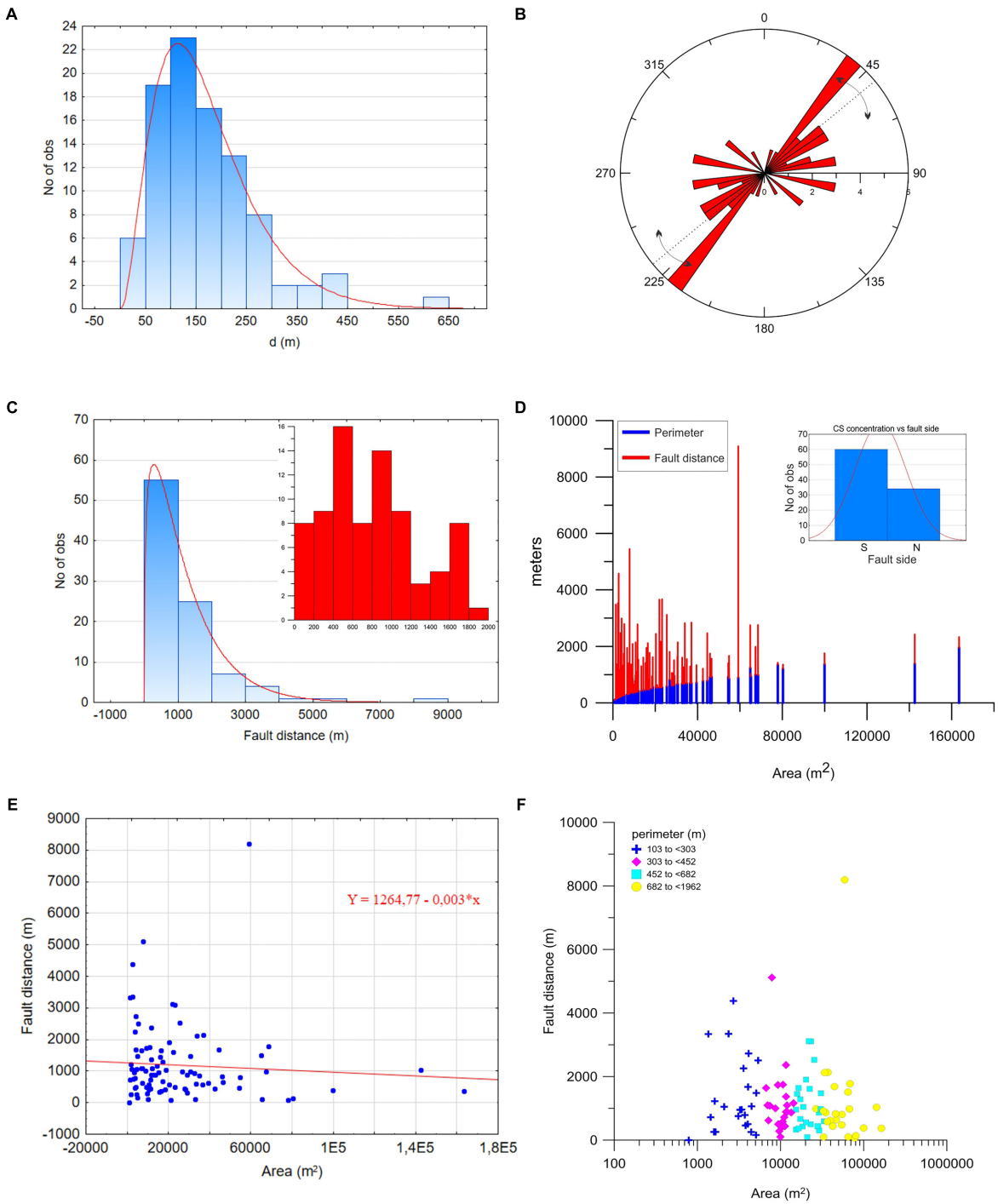

FIGURE 5 | Results of the statistical study of the mapped CS. **(A)** histogram and the corresponding fitted gamma distribution of the measured CS diameter showing that most of the structures (59 cases) have diameter ranging between 50 to 200 m, and the highest number of observations (23 cases) were recorded between 20 and 100 m in diameter; **(B)** Rose diagram indicates that the majority of the structures have an axis elongated in NE/SW direction, i.e., subparallel to the fault strike direction (indicated by dashed line as main orientation, and arrows as angle range variations); **(C)** histogram with corresponding fitted gamma distribution of CS fault distance; most of the data (55 cases) are at a distance of less than 1000 m, 25 cases are between 1000 and 2000 m, the remaining 14% is distributed between 3000 and 6000 m from the fault, and only 1 cases is found at a distance between 8000 and 9000 m. Inset shows in detail the first 2000 m of fault distance highlighting a bimodal distribution with most of CS ranging from 400–600 and 800–1000 m. **(D)** Histogram of frequency distribution of perimeter and distance from the fault in function of the CS area. The column heights are proportional to the class frequencies of both variables. Statistics suggest that both variables (fault distance and perimeter) are not stationary in the study area and that there are trends in the spatial distribution of data values. **(E)** Scatterplot of fault distance vs. area (m^2) helps to fit the function through the points to best represent the relationship between the two variables providing a linear fit equation. **(F)** The correlation among fault distance, perimeter, and area of CS highlights the presence of four perimeter population classes.

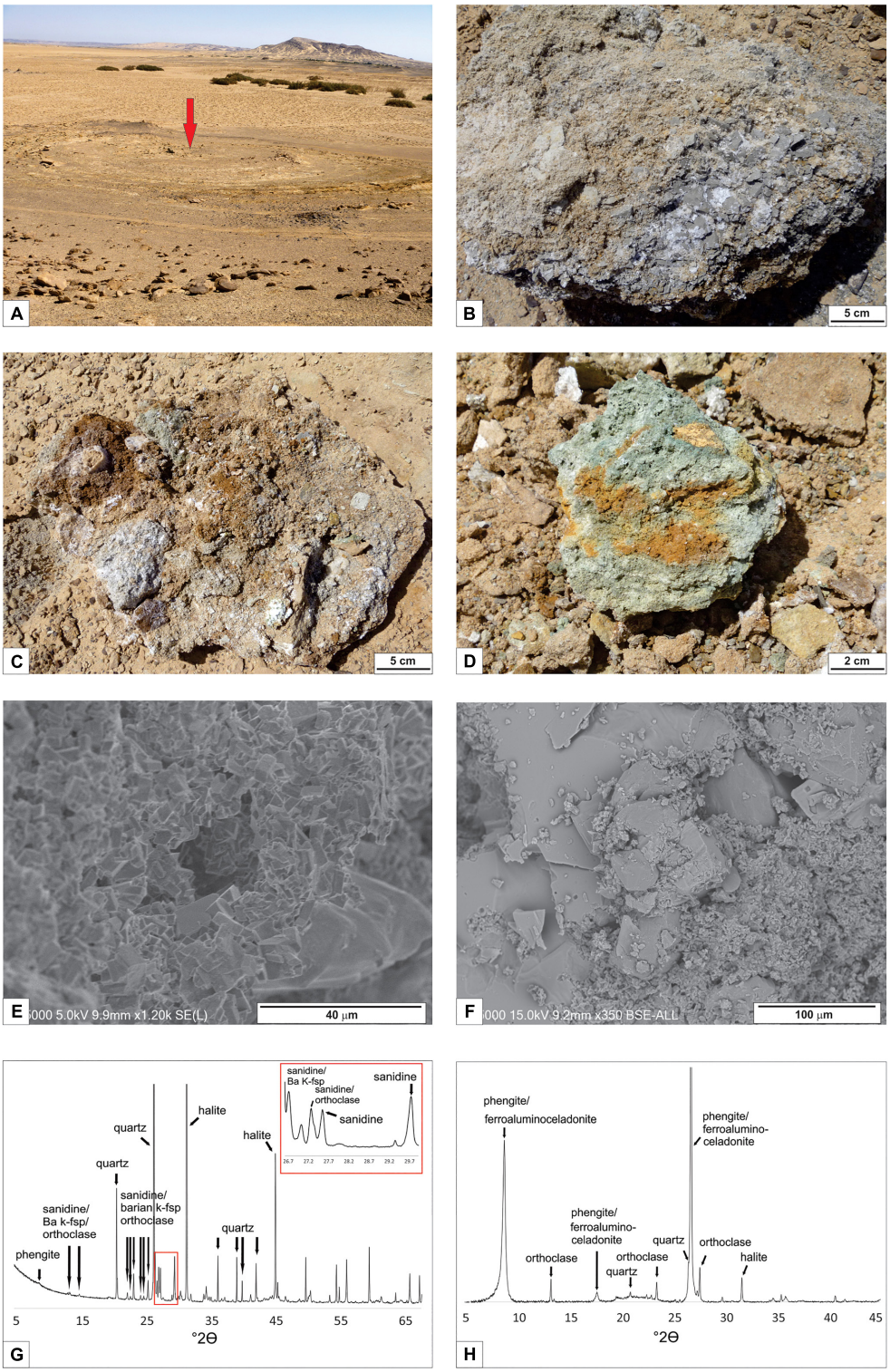

FIGURE 6 | Petrography of the central part of the CS. **(A)** Panoramic view of the central part of one CS; note the concentric rings of inward dipping sandstone and shale host rocks. The diameter of the outer circles ~20 m. Red arrow indicates the centre of the CS. **(B,C)** sediments dug out from the central part of the CS show brecciated shale and sandstone clasts within a fine-grained matrix cemented by halite (white crystals). **(D)** Detail of one of the greenish colored conduits. **(E)** SEM image of K-feldspar coated microconduit through which hydrothermal fluids promoted the precipitation of high temperature minerals. **(F)** Subrounded quartz grains and halite are overgrown by the last fine-grained GIV ferroaluminoceladonite. **(G)** XRD diagram of one of the rock samples from the central conduit of CS with the major peak positions of identified minerals. **(H)** XRD diagram of the textured sample for the identification of clay minerals (<2 µm grain size fraction). Note that the clay peak at 8.8°2θ of phengite and ferroaluminoceladonite (two 10 Å phases) becomes more evident than in the whole rock sample.

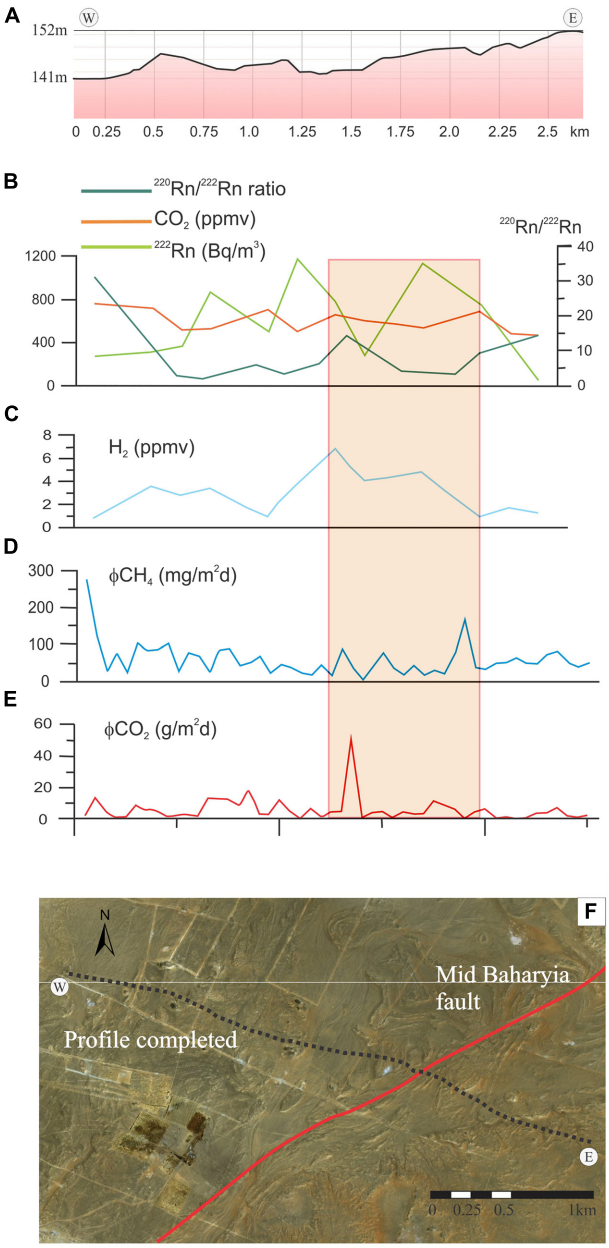

FIGURE 7 | (A) Vertical exaggerated topographic altitude of the NW-SE profile (black line); spatial distribution of **(B)** CO_2 and ^{222}Rn concentrations and $^{220}Rn/^{222}Rn$ ratio; ^{222}Rn peaks are present at the intersection with the master fault (~1.9 km), extension fault on the hanging wall (~1.2 km). **(C)** H_2 concentration, **(D)** CH_4 flux measurements, **(E)** CO_2 flux measurements. The intersection with the main trend of the master fault (red segment) and strain sector around the fault (light red shaded rectangle) are reported; **(F)** Google earth image of the NW-SE profile (black points) and fault lineament (red line).

of GI decreases from the center toward the rims within the different growth zones. In contrast with the anhedral crystals of GI and GII (**Figures 8B,C**), the last K-feldspar phase (GIII) is euhedral and displays smaller grain size (**Figures 8G–J**). Its euhedral habitus reminds of adular, but the X-ray analysis identified it as K-feldspar phase. Sanidine may be rimmed by K-feldspar generation GII and was detected by XRD and confirmed by EDS analysis with up to 5% Na_2O (Eastwood et al., 2015). In the proposed paragenetic diagram this mineral crystallizes before K-feldspar generation GII, but the context of its crystallization could not be well constrained. SEM observations of larger sample fragments from the green colored specimens (**Figure 6D**), also reveal the presence of an intricate network of microconduits that are almost entirely coated by euhedral K-feldspar (**Figure 6E**).

A textured sample was prepared to allow the identification of clay minerals (<2 μm grain size fraction; **Figure 6H**). The peak at 8.8°2θ CuKα is composed of two 10 Å phases which are phengite and ferroaluminoceladonite as confirmed by SEM and microscopy observations (**Figure 8F**). Orthoclase is the only K-feldspar phase detected in the <2 μm grain size fraction (**Figure 6G**). Ba-rich K-feldspar is not present due to its coarse-grained morphology. Preliminary microscopic observations of the brown sandstone show abundance of GI and GII K-feldspar and formation of FeO-OH alteration (**Figure 8K**) and the absence of ferroaluminoceladonite.

DISCUSSION

We have shown that large part of the CS are concentrated in a region around the Mid Bahariya fault zone and close to the volcanic outcrops. The geochemical profile carried out across the fault zone (**Figure 7**) did not provide any conclusive evidence to confirm any current sustained gas seepage. The data, however, highlight some degassing-related peaks occurring around the regions of more obvious surface deformation related to fault activity. The difficulty of collecting data in this type of setting is the strong atmosphere gas shallow circulation (e.g., average values of $^{220}Rn/^{222}Rn$ ratio, **Figure 7B**). This is typical of desert regions where highly permeable and very porous soil cover promotes the rapid dissolution and displacement of the deeper soil gas (Hinkle, 1994). Similarly, field observations and soil-gas flux measurements through the CS were not decisive to support any ongoing seepage. However, the positive variations of CO_2 and CH_4 suggest enhanced permeability in the central region of the CS. While large part of the CS consist of the same sedimentary units characterizing the BD, the central part reveal the ubiquitous presence of brecciated rocks and associated mineralogical phases. The petrographic analysis conducted on these rocks provide insights about the former processes that characterized the formation of the structures. The mineralogical associations analyzed in this study indicate the presence of primary high temperature minerals that are typically associated with the former circulation of hydrothermal fluids (Reyes, 1990). The inward dipping of the sedimentary strata inside the crater of the CS are typical of deflation phases occurring around a region of focused seepage.

In the introduction, we pointed out that several mechanisms might be able to generate concentric circular structures. For instance, some circular structures found in other planets and

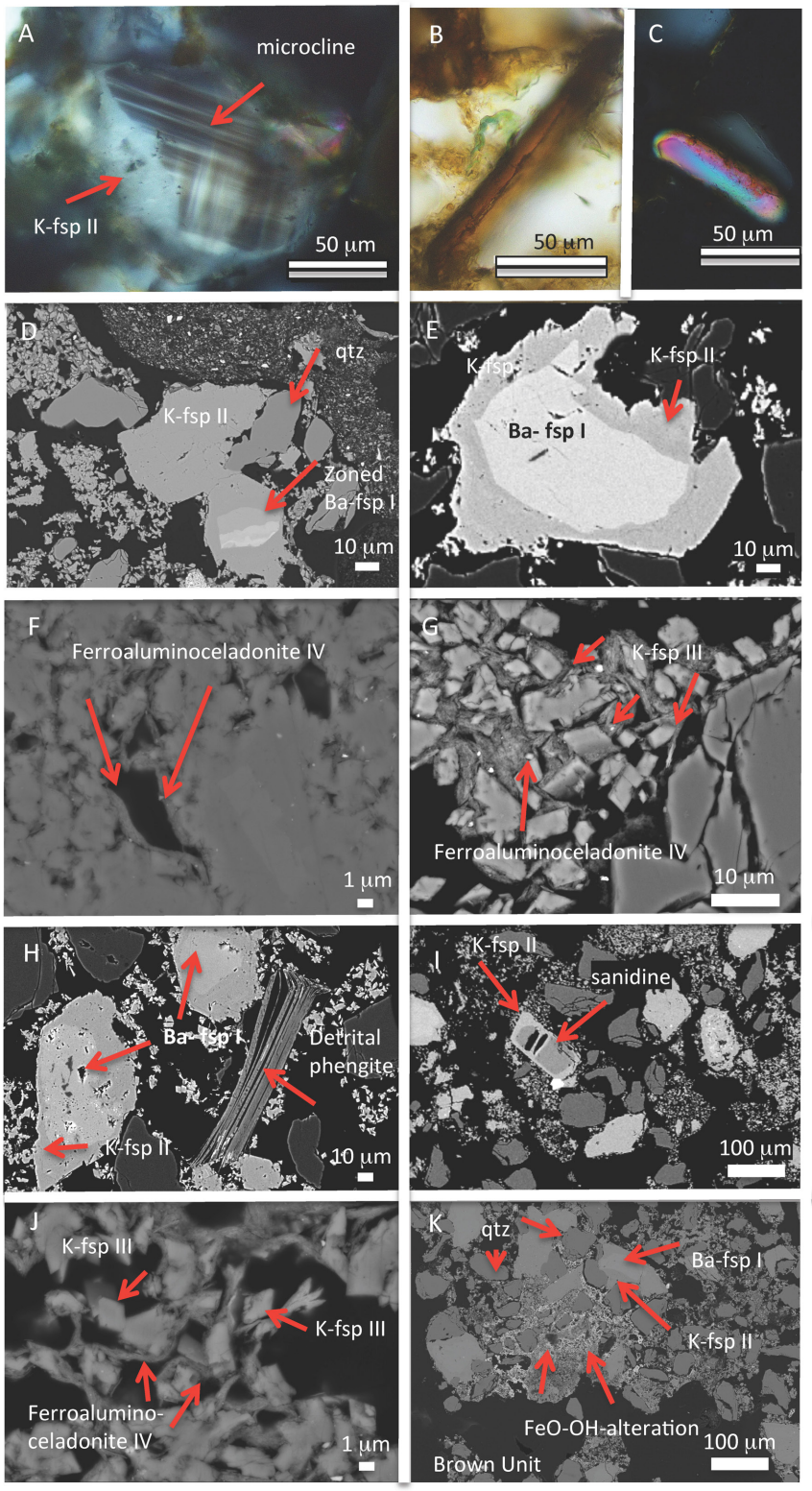

FIGURE 8 | Petrography of the analyzed rocks. **(A–C)** Microscope images. **(A)** Microcline rimmed by K-feldspar generation GII, XPL (cross-polarized light); **(B)** rutile, PPL (plane-polarized light); **(C)** zircon, XPL. **(D–K)** back scattered images. **(D)** Zoned Ba-K-feldspar I rimmed by K-feldspar II; **(E)** zoned K-feldspar with Ba-rich center I and rim ksp II; **(F)** ferroaluminoceladonite IV as the last phase to coat earlier grown minerals; **(G)** ferroaluminoceladonite IV coats last euhedral K-feldspar phase III; **(H)** detrital phengite and the three feldspar generations I to III; **(I)** sanidine with up to 5% Na_2O rimmed by K-feldspar; **(J)** last euhedral K-feldspar phase III surrounded by ferroaluminoceladonite IV; **(K)** brown unit with Fe-O-OH alteration and zoned Ba-K-feldspar.

satellites are ascribed to cryovolcanism, debris-covered impact craters filling-burial- and exhumation (Fagents, 2003; Edgett, 2005; Levy et al., 2010; Sori et al., 2017). Ice and glacier-related phenomena are not applicable in the BD. Circular structures on Mars are also described as pit craters (or pit crater chains) (Wyrick et al., 2004 and refs. therein). Several mechanisms have been proposed to explain the origin of these pit craters. Wyrick et al. (2004) provide a review indicating that these features may result from various geological processes most of which are related to subsurface migration of magma toward the surface. These processes include: lava tubes, dikes interaction with shallow hydrosphere/cryosphere layers, dikes with surficial exsolved volatiles or triggering Plinian-style eruptions, collapsed magma chambers, karst dissolution, or surface extensional fracturing and dilational faulting. Many of these processes are also observed on Earth and their applicability in our study area will be described in more detail in the following paragraphs.

On Earth, circular structures have been shown to occur in the near-field of moderate- to large-magnitude earthquakes (Tuttle, 2005). The occurrence of a long-lived and well-developed fault system would support the causal link between CS and fault slip. The paragenesis of the mineral phases illustrated above could be explained by fluid flow pervading the CS fuelled by the heat of the magmatic reservoirs at depth. However a seismic cause could not explain the brecciated units from different stratigraphic layers found in the central part of CS. Additionally, seismically promoted circular structures typically do not show any significant elevation (unlike the studied CS) and the ring features consist of homogeneous fine sediments flushed from a central zone and then expanded laterally. A similar reasoning holds also for sedimentary structures such as mud volcanoes (e.g., Mazzini and Etiope, 2017) that would explain the morphology of the CS but not reconcile with the presence of intact sedimentary units inside the crater zone and with the mineral phases identified by the petrographic study. Circular basins found across Sabah, Malaysia (Balaguru et al., 2003), have been suggested to be sedimentary basins formed due to transtensional tectonics that was favoring the development of pull-apart basins. These structures were then filled by sediments in the alternating subtidal, intertidal, and subaerial environments that characterized such regions. However, also this causal link would not help to explain the origin of the hydrothermal minerals, nor the presence of brecciated units in the center of the CS. A model invoking the karst dissolution of buried carbonate units may not be fully discarded. This mechanism, suggested to be responsible for the formation of the BD (Said, 1962; El Aref et al., 1987) could have caused the inwards dipping of the CS. Such collapse-zones could have been pervaded by fluids upwelling from depth. This model, however, does not fully conceal with the presence of the mixed brecciated sediments and the detected high temperature primary minerals. This last observation also rules out causal processes responsible for the formation of pockmarks and sedimentary/salt diapirism as well as other mechanisms that are exclusively related to surficial erosional processes (e.g., differential erosion on isoclinal anticlines and synclines folds, salt withdrawal basins). The origin of the CS related to a meteorite impact can also be excluded given the absence of impact-shattered rocks that are typically present in such craters. For these reasons Paillou et al. (2006) suggested that the CS in Gilf Kebir mapped by Paillou et al. (2004) (and initially interpreted as impact craters) could have been instead caused by hydrothermal activity. A hydrothermal origin may also help to reconcile the data presented in this study. We propose that the CS mapped in the BD were the upper termination of paleo-hydrothermal vents triggered by subsurface magmatic intrusion intercepting C-rich sediments. We argue that this scenario is supported by numerous evidences presented in this study. Several authors have shown that hydrothermal vents are characterized by brecciated mixed sediments with associated high-temperature primary minerals (e.g., Svensen et al., 2006; Polozov et al., 2016; Neumann et al., 2017) and surrounded by the local host rocks. The inward dipping of the strata observed in the CS, has been documented both in field and is seismic profiles intersecting palaeo vents that were triggered by magmatic intrusions in volcanic sedimentary basins (Jamtveit et al., 2004; Planke et al., 2005; Svensen et al., 2009; Kjoberg et al., 2017; Omosanya et al., 2018).

We propose that the CS mapped in the BD have a causal link with the hydrothermal activity promoted by magmas at depth. This interaction took place in a tectonically active setting that may have facilitated the vigorous circulation of hydrothermal fluids at depth thanks to a recurrently enhanced permeability of the upper crust (e.g., granted for instance by repeated seismic events occurring along the Mid Bahariya fault). Below we explore whether this scenario is compatible with our data combining field and petrography observations.

Hydrothermal Activity and Mineralogical Phases

The textural relationship of the mineral phases point out three generations of K-feldspars. These reflect the different timing of the proposed hydrothermal scenario:

(I) The Ba-bearing K-feldspar likely represents the first K-feldspar phase (GI) to crystallize in the conduit during hydrothermal alteration at elevated temperatures. The anhedral shape of these crystals may suggest that they were fragmented during the upwelling transport within the conduit. We cannot exclude that the formation of this Ba-bearing K-feldspar could also be related to a replacement process of barite within the sedimentary host rock during low-temperature alteration (Moro et al., 2001). The sedimentary rock was brecciated and anhedral grains of Ba-bearing K-feldspar were transported within the conduit.

(II) The Ba-bearing K-feldspar (GI) is overgrown by a Ba-free K-feldspar (GII), which probably crystallized at shallower depths within the conduit and formed at lower temperature. Rare sanidine was observed by SEM and XRD and is paragenetically occurring before the K-feldspar GII. This is normally considered a high temperature phase occurring in eruptive felsic rocks. In the observed sample, sanidine is an early phase at the beginning of hydrothermal alteration and might have formed during early brecciation in the vent.

(III) The seepage of hydrothermal fluids at shallower depth promoted the precipitation of the last euhedral K-feldspar generation (GIII) in microconduits (observed with the SEM, **Figure 6E**) through which the focused flow of hydrothermal fluids was occurring. K-feldspar generations GII and GIII show no alteration of clay minerals.

(IV) The last and locally occurring hydrothermal low temperature phase (GIV) is ferroaluminoceladonite which may have formed at temperatures as low as 50°C (Andrews, 1980; Baker et al., 2012) and we considered it as the final phase of hydrothermal fluid circulation. Fe-oxide/hydroxide is probably the product of surface alteration.

(V) Ultimately the ubiquitous and pervasive halite phase in the groundmass is also consistent with evaporation cycles occurring at the latest stages of the hydrothermal activity.

Further, insights are provided by the presence of halite-cemented clasts of different lithologies in the central part of the CS. This type of diversified deposits is typically observed at mud volcanoes and hydrothermal vent systems where mud breccia texture (i.e., consisting of a mixture of clasts of different lithologies and fine-grained sediments) characterizes the internal structure of the vertical feeder conduits (e.g., Jamtveit et al., 2004; Mazzini and Etiope, 2017). This finding suggests that processes driven by supra-lithostatic pressures were able to brecciate and possibly transport a melange of lithologies in the central part of the CS.

The sandstone beds of the Bahariya Formation are mainly carbonate-cemented (Soliman and Khalifa, 1993; Iron Exploration Project [IEP], 1994) while the same intervals within the CS are characterized by Ba-rich and ferruginous cement. Ba mineralization is also documented in fractures and faults in the carbonate rocks of the Naqb Formation (Afify, 2016). The authors interpret its formation as a mixing of late-stage hydrothermal fluid with meteoric. Other localities mentioned by Afify (2016) include veins in the South of Gebel El Haufhuf. These Ba veins trend in different directions and are associated with major fold and fault structures that are restricted to the sandstone succession of the Sabaya Formation (Bahariya). Some of these veins attain more than 7 m in length and a width ranging between 0.5 and up to 4 m (Afify, 2016). The discovered barite veins are exclusively composed of barite and quartz with barite attaining 56% by weight (Haroun and Raslan, 2010). The occurrence of barite in veins can be explained by the ascent of a relatively reducing hydrothermal fluid and mixing with oxidizing sulfate-rich surficial waters (Blount, 1977; Langmuir and Melchior, 1985). The presence of quartz within the barite veins is compatible with a temperature drop. The presence of K-feldspar and celadonite and the absence of clay minerals such as sericite or kaolinite suggest a fluid close to a neutral pH. Barium could have been leached from Ba-bearing minerals in underlying rocks and the hydrothermal fluid had to be slightly saline to effectively transport Barium (Blount, 1977; Langmuir and Melchior, 1985).

A parallel study (Sciarra et al., 2017) has been carried out on the water geochemistry of 10 water wells in the BD (**Figure 1**). 8 out of 10 wells (<1000 m deep) have shown warm water up to 52°C. The obtained geochemical signature reveals Ba-enrichment in all the wells, with peaks in those with higher temperatures. This is combined with the enrichment of other minor elements such as Zn and Rb. The presence of Ba-rich fluids (usually liberated during diagenetic and low grade metamorphic mobilization processes) at depth is consistent with the evidence of Ba mineralization documented by Afify (2016) and by the Ba-cemented host rocks surrounding the CS where the hydrothermal fluids migration is postulated.

Stratigraphic Constraints on Faulting, Volcanism and CS Dating

One of the key goals of this study was to understand if a connecting mechanism between the formation of the CS, the strike-slip system and the emplacement of the igneous effusive outcrops exists.

Based on the available data, it is not possible to well-constrain the age of the CS but it is possible to suggest that they were coeval with at least part of the activity of the fault (spanning in age from Late Cretaceous-Miocene). In fact, cross stratigraphy observations indicate that the Bahariya fault experienced three main phases of activity occurring respectively during the Late Cretaceous (88–70 Ma), Middle-Late Eocene (45–33 Ma) and Middle-Late Miocene (16–5.3 Ma) (Sehim, 1993; Moustafa et al., 2003). Available data indicate Oligocene- Lower Miocene and Middle Miocene as main periods for the volcanic events (Meneisy and El Kalioubi, 1975; Bosworth et al., 2015). The Oligocene-Miocene volcanic activity (Bosworth et al., 2015) conceivably recycled these pre-existing weak damage zones to propagate in the subsurface and ultimately manifest at the surface in the area around the fault zone. Here the formations are highly fractured and the intrusions could more easily propagate. The proposed model, embrace the well-known mechanisms that are recognized to have triggered the modern and palaeo hydrothermal vent systems. In this case, subsurface intrusions are a key element to generate the thermo-metamorphic reactions in C-rich sediments, generate overpressure at depth, and the resulting formation of CS. The cause-effect link between faulting, magmatism, and ultimately CS surface manifestation is supported by the confined geographical distribution of these three geological phenomena (i.e., with CS mapped exclusively to the south of the volcanic outcrops and mostly in the southern block of the fault, **Figure 2A**). The dominant distribution of the CS in the southern block of the Mid Bahariya fault may be due to the dip of the fault plane that would focus fluids in this region. However, given the little amount of data to address this point we do not speculate about the geographical distribution of the CS.

Figures 4B,C shows that several CS (in general proximal to the fault trace) display a NE-striking deformation subparallel to the strike of the Mid Bahariya fault. Such deformation must have occurred during the hydrothermal activity of the CS, i.e., before the final cementation phase of the structures that would have otherwise lead to brittle deformation. Some CS, however, display distinct brittle deformation (**Figure 4D**). This may indicate that part of the tectonic deformation linked to the Mid Bahariya fault

occurred at a later stage, possibly after the final CS cementation. The proposed scenario is based on the known cross-stratigraphy correlations and dating of the volcanic rocks and its endorsement would constrain the CS formation age to the Miocene.

Formation Scenario for CS

Field mapping, stratigraphic correlation, and field data reveal that the described volcanism, the formation of CS, and the fault activity were interacting phenomena during the Miocene. The conceptual model for the formation scenario for the CS is illustrated in **Figure 9**. This model is, in our opinion, the one that better reconciles field observations, statistical data, and laboratory analyses.

- The fault structures were used as pathways facilitating the rise of magmas to the surface. This created a network

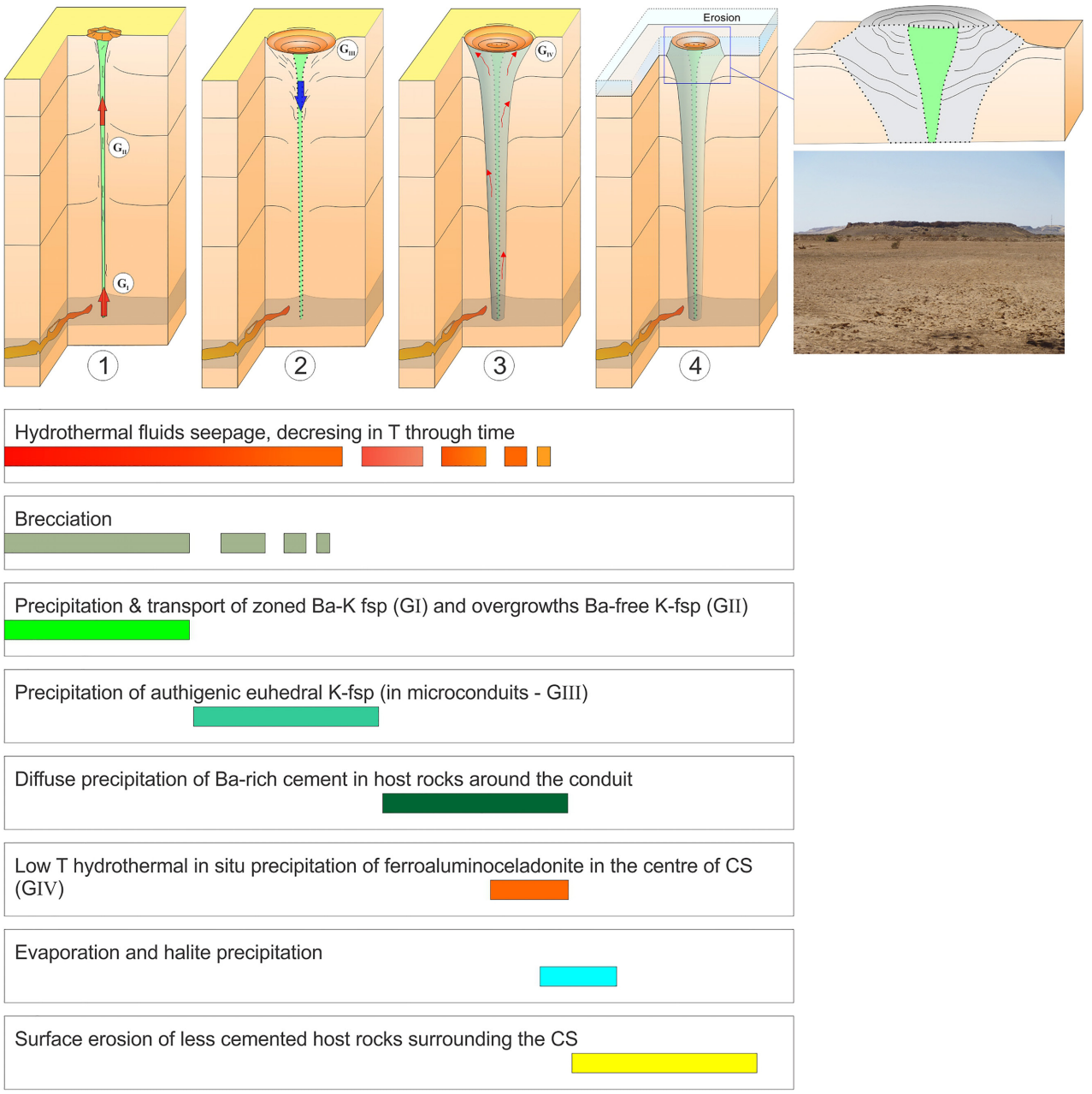

FIGURE 9 | Schematic cartoon (not to scale) of the proposed formation scenario for the CS. (1) hydrothermal venting (red arrow), brecciation of the formations within the conduit and deformation; (2) reduced venting activity, gradual sagging (blue arrow) and collapse of the conduit and inwards deformation; (3) slow hydrothermal seepage and minerals precipitation (red arrows) within the brecciated central part of the conduit and surrounding fractured areas; (4) erosion of the upper layers leaving exposed the cemented units around the crater with inwards collapse ring structures. Right: magnified crater zone and field example of CS.

of subsurface intrusions in organic-rich sediments of the lower Bahariya Fm. This emplacement initiated thermo-metamorphic reactions during the baking of the organics promoting overpressure at depth.

- The generated overpressure triggered a system of hydrothermal vents resulting in the brecciation of the stratigraphic formations intersected by the vertical conduits. Fluid circulation and further deformation occurred in the region around the pipes. The venting of hydrothermal fluids initiated the precipitation of minerals in the central regions. Permeability and porosity of the sandstone and the brecciated sediments likely have favored the precipitation of new mineral phases (**Figure 9** panel 1).
- Once the main overpressure is released, a reduced venting phase initiates. This phase is characterized by a gradual sagging and collapse of the conduits and inwards deformation of the upper part of the pipes (**Figure 9** panel 2). The created surface collapse/depression zone was likely acting as a confined basin for the expelled hydrothermal fluids that went through evaporation phase cycles. This resulted in pervasive precipitation of halite deposits within the brecciated sediments inside the conduit (**Figure 9** panel 3). During this phase a pervasive diffusion of high temperature fluids occurred within the host rocks (mainly sandstones) encasing the vent conduit.
- During the latest venting phase, hydrothermal fluids were still vertically upwelling through the conduit. Additional lateral fluid migration promoted the cementation of the surrounding host rocks with Ba-rich minerals in the aureole zone of the CS. This molded the last stage of morphology and mineralogy of the active system (**Figure 9** panel 3).
- A final surface erosion phase of the upper layers left exposed the cemented units around the crater where the collapse dip is observed (**Figure 9** panel 3).

Modern and Fossil Hydrothermal Vent Systems on Earth

Hydrothermal vent systems on Earth have been focus of attention of numerous projects during the last decades. These systems are extremely relevant as they exhibit the surface expression of overpressure created at depth and represent an open window to decipher the deep reactions and dynamics of our planet. Understanding the mechanisms controlling these geological phenomena is also important to unravel the climatic crises that characterized our planet in the geological past, as well as their current impact at regional scale and in the global planetary budget.

Classic fossil examples of these hybrid systems are documented in southern Australia (Middle-Eocene) in the North Atlantic (Paleocene-Eocene), in South Africa (Early Jurassic) and Siberia (end-Permian) (e.g., Jamtveit et al., 2004; Svensen et al., 2004, 2007, 2009; Reynolds et al., 2017a,b). In these regions the emplacement of Large Igneous Provinces (LIPS) within vast sedimentary basins created a network of igneous intrusions extending across $>$500,000 km^2, partly in carbon-rich sedimentary rocks. The interaction between magma and the sedimentary rocks generated overpressure of C-rich gas released in the atmosphere through thousands of vents. A wealth of scientific evidence indicates that such rapid release of sediment-derived ^{12}C-enriched gas to the atmosphere may have contributed to triggering rapid climate change and extinction events since 260 Ma (Svensen et al., 2018 and references therein). Active hydrothermal vent systems, driven by the same processes as described above, are also currently active on Earth and are termed sediment-hosted hydrothermal systems (Mazzini and Etiope, 2017; Procesi et al., 2019). Currently, active sites are documented in the Guaymas Basin Rift Zone-Gulf of California (Pacific Ocean), in the Salton Sea geothermal field (California), within the Tiber Delta, at Fiumicino (central Italy), and in the Songliao Basin (northern China) (e.g., Helgeson, 1968; Welhan and Lupton, 1987; Mazzini et al., 2011; Berndt et al., 2016; Ciotoli et al., 2016; Shuai et al., 2018; Procesi et al., 2019). Today the largest active vent system is the Indonesian Lusi eruption (active since May 2006) that has been targeted by numerous multidisciplinary studies to fill the knowledge gap between modern and ancient hybrid systems (e.g., Mazzini et al., 2012; Fallahi et al., 2017; Lupi et al., 2018; Malvoisin et al., 2018; Mazzini, 2018; Miller and Mazzini, 2018).

The finding of a new hydrothermal vent complex in the BD (Western Sahara) represents a new documentation of hydrothermal vent activity in the African continent. Further investigations at this locality are needed to constraint the age of the activity and reconstruct the timing of the geological processes. A potential link between the Miocene magmatism and the opening of the Red Sea and the CS activity in BD cannot be excluded and represent a promising topic for future studies.

CONCLUSION

A field campaign conducted in the Bahariya Depression, Western Desert, Egypt, investigated the presence of nearly a hundred sub-circular concentric structures. These reach a diameter of up to 625 m and are located close to a well-developed strike-slip fault system (Bahariya Fault) and magmatic outcrops. We conducted a multidisciplinary study combining geological field survey, geochemical sampling and petrographic studies to shed light on the origin of these structures. We considered processes that may have generated concentric structures on Earth and other planets and satellites, and propose that hydrothermal venting is the most likely mechanism responsible for the formation of such concentric structures in the Bahariya Depression. In particular, we highlight how several geological processes promoted each other in a chain of events that resulted in the formation of these enigmatic features. Based on geological and stratigraphic correlations we propose a Miocene age for these concentric structures that are coeval with one of the activity phases of the Mid Bahariya fault. Miocene magmatism, possibly linked with the opening of the Red Sea, resulted in surface eruptions and subsurface magmatic intrusions. The latter propagated

along fractured zones and triggered thermo-metamorphic processes within the carbon-rich sediments of the Bahariya Fm. generating a large amount of gas and overpressure at depth. These supra-lithostatic pore pressures conditions promoted the brecciation and upwelling of deep fluids through newly generated hydrothermal vents that today crop out as large circular concentric structures. Brecciated sediments are present in the central part of the crater sites. Laboratory analyses confirmed the presence of high temperature minerals, including three K-feldspar generations. Next, weathering and erosion removed the upper units hosting the hydrothermal vents leaving exposed the cemented concentric structures. These structures may represent one of the very few examples of paleo- sediment-hosted hydrothermal systems in the region. Further studies will be necessary to constrain the evolution of the Bahariya in the past and help deciphering the interaction between magmatic bodies and sedimentary basins.

DATA AVAILABILITY STATEMENT

The datasets analyzed in this manuscript are not publicly available. Requests to access the datasets should be directed to AM, adriano.mazzini@geo.uio.no.

AUTHOR CONTRIBUTIONS

All authors actively contributed to various parts of the manuscript and agreed with its contents. AM, ML, AlS, and MH collected the data on the field and developed the concept of the manuscript. AM, SS, AnS completed the petrograpic analyses on the samples and contributed to their interpretation.

FUNDING

This work was partially supported by the Swiss National Fund (project PZ00P2_154815), the European Research Council under the European Union's Seventh Framework Programme Grant agreement n° 308126 (LUSI LAB project, PI AM), and the Research Council of Norway through its Centers of Excellence funding scheme, Project Number 223272 (CEED). ML is a SCCER-SoE Professor and thanks the KTI for financial support.

ACKNOWLEDGMENTS

We wish to thank the editor and the reviewers who greatly contributed to improve this manuscript.

REFERENCES

Afify, A. M. (2016). *Ironstone Occurrences in the Northern Part of the Bahariya Depression, Western Desert, Egypt: Geology, Mineralogy, Geochemistry and Origin*. PhD Dissertation. Spain: Universidad Complutense De Madrid, 167.

Andrews, A. J. (1980). Saponite and celadonite in layer 2 basalts, DSDP Leg 37. *Contrib. Mineral. Petrol.* 73, 323–340. doi: 10.1007/bf00376627

Baker, L. L., Rember, W. C., Sprenke, K. F., and Strawn, D. G. (2012). Celadonite in continental flood basalts of the Columbia River Basalt Group. *Am. Mineral.* 97, 1284–1290. doi: 10.2138/am.2012.4129

Balaguru, A., Nichols, G. J., and Hall, R. (2003). The origin of the circular basins of Sabah, Malaysia. *Geol. Soc. Malaysia Bull.* 46, 335–351. doi: 10.7186/bgsm46200355

Barakat, A. (1994). El-Baz Crater: basaltic intrusion versus meteoritic impact crater. *Ann. Geol. Surv. Egypt* 24, 167–177.

Basta, E. Z., and Amer, H. I. (1969). El Gedida iron ores and their origin, Bahariya oasis, Western Desert, U.A.R. *Econ. Geol.* 64, 424–444. doi: 10.2113/gsecongeo.64.4.424

Berndt, C., Hensen, C., Mortera-Gutierrez, C., Sarkar, S., Geilert, S., Schmidt, M., et al. (2016). Rifting under steam—How rift magmatism triggers methane venting from sedimentary basins. *Geology* 44, 767–770. doi: 10.1130/g38049.1

Blount, C. W. (1977). Barite solubilities and thermodynamic quantities up to 300°C and 1400 bar. *Am. Mineral.* 62, 942–957.

Bosworth, W., Stockli, D., and Helgeson, D. (2015). Integrated outcrop, 3D seismic, and geochronologic interpretation of Red Sea dike-related deformation in the Western Desert, Egypt – The role of the 23 Ma Cairo "mini-plume". *J. Afr. Earth Sci.* 109, 107–119. doi: 10.1016/j.jafrearsci.2015.05.005

Cardellini, C., Chiodini, G., and Frondini, F. (2003). Application of stochastic simulation to CO2 flux from soil: mapping and quantification of gas release. *J. Geophys. Res.* 108, 2425–2438.

Catuneanu, O., Khalifa, M. A., and Wanas, H. A. (2006). Sequence stratigraphy and incised-valley systems of the Cenomanian Bahariya Formation, Western Desert, Egypt. *Sediment. Geol.* 190, 121–137. doi: 10.1016/j.sedgeo.2006.05.010

Ciotoli, G., Etiope, G., Marra, F., Florindo, F., Giraudi, C., and Ruggiero, L. (2016). Tiber delta CO2-CH4 degassing: a possible hybrid, tectonically active sediment-hosted geothermal system near Rome. *J. Geophys. Res. Solid Earth* 121, 48–69. doi: 10.1002/2015JB012557

Clayton, P. A. (1933). The western side of the Gilf Kebir. *Geogr. J.* 81, 254–259.

Dominik, W. (1985). Stratigraphie und Sedimentologie (Geochemie, Schwermineralanalyse) der Oberkreide von Bahariya und ihre Korrelation zum Dakhla Becken (Western Desert, Agypten). *Berliner Geowissenschaftliche Abhandlungen* 62, 173.

Eastwood, A., Oze, C., Fraser, J., Cole, G. D., Chambefort, I., and Gordon, K. C. (2015). Application of Raman spectroscopy to distinguish adularia and sanidine in drill cuttings from the Ngatamariki geothermal Field, New Zealand, New Zealand. *J. Geol. Geophys.* 58, 66–77. doi: 10.1080/00288306.2014.991744

Edgett, K. S. (2005). The sedimentary rocks of Sinus Meridiani: five key observations from data acquired by the Mars Global Surveyor and Mars Odyssey orbiters. *Int. J. Mars Sci. Explor.* 1, 5–58. doi: 10.1555/mars.2005.0002

El Akkad, S., and Issawi, B. (1963). Geology and iron ore deposits of the Bahariya Oasis. *Geol. Surv. Egypt Cairo* 18, 301.

El Aref, M. M., AbouKhadrah, M. A., and Lotfi, Z. H. (1987). Karst topography and karstification processes in the Eocene limestone plateau of El Bahariya Oasis, Western Desert, Egypt. *J. Geomorph.* 31, 45–64.

El Aref, M. M., El Dougdog, A. A., and Mesaed, A. A. (1991). Landform evolution and formation of Ferricrete Duricrusts, El Heiz Area, El Bahariya Depression, Western Desert, Egypt. *J. Geol.* 34, 1–39.

El Aref, M. M., El Sharkawi, M. A., and Khalil, M. (1999). "Geology and genesis of the stratabound and stratiform cretaceous - eocene iron ore deposits of El Bahariya Region, Western Desert, Egypt," in *Proceedings of the 4th International Conference on Geology of the Arab World*, (Egypt: Cairo University), 450–475.

El Aref, M. M., Hammed, M. S., and Salama, A. (2017). Inventory and Assessment of the Geomorphosites of Bahariya –Farafra Territory, Western Desert, Egypt. *Int. J. Sci. Basic Appl. Res.* 33, 128–143.

El Nagar, H. (2012). *Structural architecture of Bahariya Oasis, Western Desert, Egypt*. MSc thesis, Cairo: Al Azhr University, 1–158.

El Qaluabi, B. (1974). *Petrological Study on the Volcanic Rocks of Bahariya Oasis*. MSc thesis. Cairo: Ain Shams University, 129.

El Sisi, Z., Hassaouba, M., Odani, M. J., and Dolson, J. C. (2002). *The Geology of Bahariya Oasis in the Western Desert of Egypt and its Archeological Heritage*. Tulsa, OK: AAPG.

Ezzelarab, M., Ebraheem, M. O., and Zahradnik, J. (2018). A recent Mw 4.3 earthquake proving activity of a shallow strike-slip fault in the northern part

of the Western Desert, Egypt. *J. Afr. Earth Sci.* 139, 275–282. doi: 10.1016/j.jafrearsci.2017.12.021

Fagents, S. A. (2003). Considerations for effusive cryovolcanism on Europa: the post-Galileo perspective. *J. Geophys. Res. Planets* 108:E12.

Fallahi, M. J., Obermann, A., Lupi, M., Karyono, K., and Mazzini, A. (2017). The plumbing system feeding the Lusi Eruption revealed by ambient noise tomography. *J. Geophys. Res. Solid Earth* 122, 8200–8213. doi: 10.1002/2017jb014592

Franks, J. R. (1982). "Stratigraphic modelling of the upper cretaceous sediments of Bahariya Oases," in *Proceedings of the 6th Egyptian General Petroleum Corporation Seminar*, (Cairo), 93–105.

Grotzinger, J., Jordan, T. H., Press, F., and Siever, R. (2007). *Understanding Earth*, 5th Edn. New York: W. H. Freeman, 672.

Haroun, Y. S., and Raslan, M. F. (2010). Occurrence of barite mineralization in Bahariya depression, Western Desert, Egypt. *Physicochem. Probl. Minerol. Process.* 44, 41–52.

Helgeson, H. C. (1968). Geologic and thermodynamic characteristics of Salton Sea geothermal system. *Am. J. Sci.* 266, 129–166. doi: 10.2475/ajs.266.3.129

Hinkle, M. E. (1994). Environmental conditions affecting concentrations of He, CO2, O2 and N2 in soft gases. *Appl. Geochem.* 9, 53–63. doi: 10.1016/0883-2927(94)90052-3

Hutchinson, G. L., Livingston, G. P., Healy, R. W., and Striegl, R. G. (2000). Chamber measurement of surface-atmosphere trace gas exchange: numerical evaluation of dependence on soil, interfacial layer, and source/sink properties. *J. Geophys. Res. Atmos.* 105, 8865–8875. doi: 10.1029/1999jd901204

Iron Exploration Project [IEP], (1994). *Accounting Joint Project Between Cairo University and Egyptian Geological Survey and Mining Authority*. Internal report 398.

Ismail, M. M., El Nozahy, F. A., and Sadeek, K. N. (1989). A contribution to the geology of the Bahariya Oasis, Western Desert, Egypt: part 1: microfacies of the upper cretaceous-eocene succession. *GeoJournal* 18, 379–391. doi: 10.1007/bf00772692

Issawi, B. (1972). Review of upper cretaceous-lower tertiary stratigraphy in the central and northern Egypt. *Am. Assoc. Petrol. Geol. Bull.* 56, 1448–1463.

Jamtveit, B., Svensen, H., Podladchikov, Y., and Planke, S. (2004). Hydrothermal vent complexes associated with sill intrusions in sedimentary basins. *Geol. Soc. Lond. Spec. Publ.* 234, 233–241. doi: 10.1144/gsl.sp.2004.234.01.15

Khalaf, E., and Hammed, M. S. (2016). Morphology and development of pahoehoe flow-lobe tumuli and associated features from a monogenetic basaltic volcanic field, Bahariya Depression, Western Desert, Egypt. *J. Afr. Earth Sci.* 113, 165–180. doi: 10.1016/j.jafrearsci.2015.10.010

Khalaf, E. Z., Abdel Wahed, M., Maged, A., and Mokhtar, H. (2018). Volcanic geosites and their geoheritage values preserved in monogenetic neogene volcanic field, bahariya depression, Western Desert, Egypt: implication for climatic change-controlling volcanic eruption. *Geoheritage* 11, 855–873. doi: 10.1007/s12371-018-0336-6

Khalifa, M. A., Soliman, H. D., and Abu El-Hassan, M. M. (2002). "Lithostratigraphy and Sequence Stratigraphy of the Turonian–Santonian Rocks, Bahariya Oasis, Western Desert, Egypt," in *Proceedings of the 6th Conference Geology Arab World*. (Giza: Cairo University), 483–501.

Khalifa, M. A., Wanas, H. A., and Tsirambides, A. (2003). "Depositional history of the clastic-carbonate facies (El Reis Formation) of the Limestone Hills, central part of the Bahariya Oasis, Western Desert, Egypt," in *Proceedings of the 5th International Conference of the Middle East*, (Cairo: Ain Shams University), 355–366.

Kjoberg, S., Schmiedel, T., Planke, S., Svensen, H. H., Millett, J. M., Jerram, D. A., et al. (2017). 3D structure and formation of hydrothermal vent complexes at the Paleocene-Eocene transition, the Møre Basin, mid-Norwegian margin. *Interpretation* 5, SK65–SK81.

Klitzsch, E., List, F. K., and Pohlmann, G. (1987). *Geologic Map of Egypt 1:500000, Bir Misaha sheet*. Cairo: The Egyptian General Petroleum Corporation.

Langmuir, D., and Melchior, D. (1985). The geochemistry of Ca, Sr, Ba and Ra sulfates in some deep brines from the Palo Duro Basin, Texas. *Geochim. Cosmochim. Acta* 11, 2423–2432. doi: 10.1016/0016-7037(85)90242-x

Levy, J., Head, J. W., and Marchant, D. R. (2010). Concentric crater fill in the northern mid-latitudes of Mars: formation processes and relationships to similar landforms of glacial origin. *Icarus* 209, 390–404. doi: 10.1016/j.icarus.2010.03.036

Lucia, F. J. (1995). "Lower Paleozoic cavern development, collapse, and dolomitization, Franklin Mountains, El Paso, Texas," in *Unconformities and Porosity in Carbonate Strata*, Vol. 63, eds D. A. Budd, A. H. Saller, and P. M. Harris, (Tulsa, OK: AAPG), 279–300.

Lupi, M., Mazzini, A., Sciarra, A., Collignon, M., Schmid, D. W., Husein, A., et al. (2018). Enhanced hydrothermal processes at the new-born Lusi eruptive system, Indonesia. *J. Volcanol. Geotherm. Res.* 366, 47–57. doi: 10.1016/j.jvolgeores.2018.09.006

Malvoisin, B., Mazzini, A., and Miller, S. A. (2018). Deep hydrothermal activity driving the Lusi mud eruption. *Earth Planet. Sci. Lett.* 497, 42–49. doi: 10.1016/j.epsl.2018.06.006

Matton, G., Jébrak, M., and Lee, J. K. W. (2005). Resolving the Richat enigma: doming and hydrothermal karstification above an alkaline complex. *Geology* 33, 665–668. doi: 10.1130/g21542ar.1

Mazzini, A. (2018). 10 years of Lusi eruption: lessons learned from multidisciplinary studies (LUSI LAB). *Mar. Petrol. Geol.* 90, 1–9. doi: 10.1016/j.marpetgeo.2017.12.025

Mazzini, A., and Etiope, G. (2017). Mud volcanism: an updated review. *Earth Sci. Rev.* 168, 81–112. doi: 10.1016/j.earscirev.2017.03.001

Mazzini, A., Etiope, G., and Svensen, H. (2012). A new hydrothermal scenario for the 2006 Lusi eruption, Indonesia. Insights from gas geochemistry. *Earth Planet. Sci. Lett.* 317, 305–318. doi: 10.1016/j.epsl.2011.11.016

Mazzini, A., Svensen, H., Etiope, G., Onderdonk, N., and Banks, D. (2011). Fluid origin, gas fluxes and plumbing system in the sediment-hosted Salton Sea Geothermal System (California, USA). *J. Volcanol. Geotherm. Res.* 205, 67–83. doi: 10.1016/j.jvolgeores.2011.05.008

Mazzini, A., Svensen, H. H., Forsberg, C. F., Linge, H., Lauritzen, S.-E., Haflidason, H., et al. (2017). A climatic trigger for the giant Troll pockmark field in the northern North Sea. *Earth Planet. Sci. Lett.* 464, 24–34. doi: 10.1016/j.epsl.2017.02.014

McDonnell, A., Loucks, R. G., and Dooley, T. (2007). Quantifying the origin and geometry of circular sag structures in northern Fort Worth Basin, Texas: paleocave collapse, pull-apart fault systems, or hydrothermal alteration? *AAPG Bull.* 91, 1295–1318. doi: 10.1306/05170706086

Medani, A. A. (1995). *The Basaltic Rocks of the Northern Part of the Bahariya Oasis, Western Desert, Egypt. M.Sc. thesis*. Giza: Cairo University, 104.

Melosh, H. J., and Ivanov, B. A. (1999). Impact crater collapse. *Annu. Rev. Earth Planet. Sci.* 27, 385–415. doi: 10.1146/annurev.earth.27.1.385

Meneisy, M. Y. (1990). "Vulcanicity," in *The Geology of Egypt*, ed. R. Said, (Rotterdam: Balkema), 157–174.

Meneisy, M. Y., and El Kalioubi, B. (1975). Isotopic ages of the volcanic rocks of the Bahariya Oasis. *Ann. Geol. Surv. Egypt* 5, 119–122.

Miller, S. A., and Mazzini, A. (2018). More than ten years of Lusi: a review of facts, coincidences, and past and future studies. *Marine and Petroleum Geology* 90, 10–25. doi: 10.1016/j.marpetgeo.2017.06.019

Ministry of Public Works and Water Resources [MPWWR] (1998). *Ministry of Public Works and Water Resources, Hydrogeology of Deep Aquifers in the Western Desert and Sinai; Water Policy Reform Program, International Resources Group Winrock International, Nile Consultants, Report No. 10*.

Moro, M. C., Cembranos, M. L., and Fernandez, A. (2001). Celsian, (Ba,K)-feldspar and cymrite from sedex barite deposits of Zamora, Spain. *Can. Mineral.* 39, 1039–1051. doi: 10.2113/gscanmin.39.4.1039

Moustafa, A. R., Saoudi, A., Ibrahim, I. M., Molokhia, H., and Schwartz, B. (2003). Structural setting and tectonic evolution of the Bahariya Depression, western Desert, Egypt. *Geo Arabia, Bahrain* 8, 91–124.

Nakhla, F. M. (1961). The iron ore deposits of El-Bahariya oasis, Egypt. *Econ. Geol.* 56, 1103–1111. doi: 10.2113/gsecongeo.56.6.1103

Neumann, E.-R., Svensen, H. H., Polozov, A. G., and Hammer, Ø (2017). Formation of Si-Al-Mg-Ca-rich zoned magnetite in an end-Permian phreatomagmatic pipe in the Tunguska Basin, East Siberia. *Mineral. Depos.* 52, 1205–1222. doi: 10.1007/s00126-017-0717-9

Omosanya, K. O., Eruteya, O. E., Siregar, E. S. A., Zieba, K. J., Johansen, S. E., Alves, T. M., et al. (2018). Three-dimensional (3-D) seismic imaging of conduits and radial faults associated with hydrothermal vent complexes (Vøring Basin, Offshore Norway). *Mar. Geol.* 399, 115–134. doi: 10.1016/j.margeo.2018.02.007

Paillou, P., El Barkooky, A., Barakat, A., Male'zieux, J.-M., Reynard, B., Dejax, J., et al. (2004). Discovery of the largest crater field on Earth in the Gilf Kebir

region, Egypt. *C. R. Acad. Sci. Paris Geosci.* 336, 1491–1500. doi: 10.1016/j.crte.2004.09.010

Paillou, P., Reynard, B., Malézieux, J.-M., Dejax, J., Heggy, E., Rochette, P., et al. (2006). An extended field of crater-shaped structures in the Gilf Kebir region, Egypt: observations and hypotheses about their origin. *J. Afr. Earth Sci.* 46, 281–299. doi: 10.1016/j.jafrearsci.2006.05.006

Parrot, J., and Taud, T. (1992). Detection and classification of circular structures on spot images. *IEEE Trans. Geosci. Remote Sens.* 30, 996–1005. doi: 10.1109/36.175334

Planke, S., Rassmussen, T., Rey, S. S., and Myklebust, R. (2005). "Seismic characteristics and distribution of volcanic intrusions and hydrothermal vent complexes in the Vøring and Møre basins: petroleum geology: North-West Europe and global perspectives," in *Proceedings of the 6th Petroleum Geology Conference*, London, 833–844. doi: 10.1144/0060833

Plyusnina, E. E., Sallam, E. S., and Ruban, D. A. (2016). Geological heritage of the Bahariya and Farafra oases, the central Western Desert, Egypt. *J. Afr. Earth Sci.* 116, 151–159. doi: 10.1016/j.jafrearsci.2016.01.002

Polozov, A. G., Svensen, H. H., Planke, S., Grishina, S. N., Fristad, K. E., and Jerram, D. A. (2016). The basalt pipes of the Tunguska Basin (Siberia, Russia): high temperature processes and volatile degassing into the end-Permian atmosphere. *Palaeogeogr. Palaeoclimatol. Palaeoecol.* 441, 51–64. doi: 10.1016/j.palaeo.2015.06.035

Procesi, M., Ciotoli, G., Mazzini, A., and Etiope, G. (2019). Sediment-hosted geothermal systems: review and first global mapping. *Earth Sci. Rev.* 192, 529–544. doi: 10.1016/j.earscirev.2019.03.020

Reimann, E., and Filzmoser, P. (2000). Normal and log normal data distribution in geochemistry: death of a myth, Conseguences for the statistical treatment of geochemical and environmental data. *Environ. Geol.* 39, 1001–1014. doi: 10.1007/s002549900081

Reyes, A. G. (1990). Petrology of Philippine geothermal systems and the application of alteration mineralogy to their assessment. *J. Volcanol. Geotherm. Res.* 43, 279–309. doi: 10.1016/0377-0273(90)90057-m

Reynolds, P., Holford, S., Schofield, N., and Ross, A. (2017a). The shallow depth emplacement of mafic intrusions on a magma-poor rifted margin: an example from the Bight Basin, southern Australia. *Mar. Petrol. Geol.* 88(Suppl. C), 605–616. doi: 10.1016/j.marpetgeo.2017.09.008

Reynolds, P., Planke, S., Millett, J. M., Jerram, D. A., Trulsvik, M., Schofield, N., et al. (2017b). Hydrothermal vent complexes offshore Northeast Greenland: a potential role in driving the PETM. *Earth Planet. Sci. Lett.* 467, 72–78. doi: 10.1016/j.epsl.2017.03.031

Said, R. (1962). *The Geology of Egypt, Amsterdam*. Oxford: Elsevier Publ. Co, 37.

Said, R. (1990). *The Geology of Egypt*. Rotterdam/Brookfield: A.A. Balkema, 734.

Sandford, K. S. (1935). The wadi hawa. *Geogr. J.* 85, 412–431.

Sciarra, A., Mazzini, A., Lupi, M., and Hammed, M. S. (2017). *Geochemical Water Signature in the Bahariya Depression,Western Desert, Egypt*. Vienna: EGU General Assembly.

Sehim, A. A. (1993). Cretaceous tectonics in Egyptian. *J. Geol.* 37, 335–372.

Shuai, Y. H., Etiope, G., Zhang, S. C., Douglas, P. M. J., Huang, L., and Eiler, J. M. (2018). Methane clumped isotopes in the Songliao Basin (China): new insights into abiotic vs. biotic hydrocarbon formation. *Earth Planet. Sci. Lett.* 482, 213–221. doi: 10.1016/j.epsl.2017.10.057

Soliman, H. E., and Khalifa, M. A. (1993). Stratigraphy, facies and depositional environments of the Lower Cenomanian Bahariya Formation, Bahariya Oasis, Western Desert, Egypt. *Egypt. J. Geol.* 37, 193–209.

Sori, M. M., Byrne, S., Bland, M. T., Bramson, A. M., Ermakov, A. I., Hamilton, C. W., et al. (2017). The vanishing cryovolcanoes of Ceres. *Geophys. Res. Lett.* 44, 1243–1250. doi: 10.1002/2016gl072319

Stewart, S. A. (2015). Circular geological structures outcropping in the sedimentary basins of Saudi Arabia. *J. Asian Earth Sci.* 106, 95–118. doi: 10.1016/j.jseaes.2015.02.031

Stromer, E. (1914). Die topographie und geologie der strecke Gharaq-Baharije Ausfuhrungen ueber die geologische Geschichte Aegyptens. *Abhandlung Bayrischer Akademischer Wissenschaften. Mathematisch-Naturwissenschaftliche Kl* 11, 1–78.

Svensen, H., Jamtveit, B., Planke, S., and Chevallier, L. (2006). Structure and evolution of hydrothermal vent complexes in the Karoo Basin, South Africa. *J. Geol. Soc.* 163, 671–682. doi: 10.1144/1144-764905-037

Svensen, H., Planke, S., Chevallier, L., Malthe-Sørenssen, A., Corfu, F., and Jamtveit, B. (2007). Hydrothermal venting of greenhouse gases triggering Early Jurassic global warming. *Earth Planet. Sci. Lett.* 256, 554–566. doi: 10.1016/j.epsl.2007.02.013

Svensen, H., Planke, S., Malthe-Sørenssen, A., Jamtveit, B., Myklebust, R., Eidem, T., et al. (2004). Release of methane from a volcanic basin as a mechanism for initial Eocene global warming. *Nature* 429, 542–545. doi: 10.1038/nature02566

Svensen, H., Planke, S., Polozov, A. G., Schmidbauer, N., Corfu, F., Podladchikov, Y. Y., et al. (2009). Siberian gas venting and the end-Permian environmental crisis. *Earth Planet. Sci. Lett.* 277, 490–500. doi: 10.1016/j.epsl.2008.11.015

Svensen, H. H., Planke, S., Neumann, E.-R., Aarnes, I., Marsh, J. S., Polteau, S., et al. (2018). "Sub-volcanic intrusions and the link to global climatic and environmental changes," in *Physical Geology of Shallow Magmatic Systems: Dykes, Sills and Laccoliths*, eds C. Breitkreuz, and S. Rocchi, (Cham: Springer International Publishing), 249–272. doi: 10.1007/978-3-319-14084-1_10

Tanner, L. T., and Khalifa, M. (2010). Origin of ferricretes in fluvial-marine deposits of the lower cenomanian bahariya formation, Bahariya Oasis, Western Desert: Egypt. *J. Afr. Earth Sci.* 56, 179–189. doi: 10.1016/j.jafrearsci.2009.07.004

Tewksbury, B. J., Abdelsalam, M. G., Tewksbury-Christle, C. M., Hogan, J. P., Jerris, T. J., and Pandey, A. (2009). Reconnaissance study of domes and basins in Tertiary sedimentary rocks in the Western Desert of Egypt using high resolution satellite imagery. *Geol. Soc. Am.* 41:458.

Tewksbury, B. J., Dokmak, A. A. K., Tarabees, E. A., and Mansour, A. S. (2012). "Google Earth and geologic research in remote regions of the developing world; an example from the Western Desert of Egypt," in *Google Earth and Virtual Visualizations in Geoscience Education and Research*, eds S. J. Whitmeyer, J. E. Bailey, D. G. De Paor, and T. Ornduff, (Boulder, CO: Geological Society of America), 23–36. doi: 10.1130/2012.2492(02)

Tewksbury, B. J., Hogan, J. P., Kattenhorn, S. A., Mehrtens, C. J., and Tarabees, E. A. (2014). Polygonal faults in chalk: insights from extensive exposures of the Khoman Formation, Western Desert, Egypt. *Geology* 42, 479–482. doi: 10.1130/g35362.1

Tosson, S. (1964). The volcanic rocks of Bahariya Oasis, Egypt. *Bull. Volcanol.* 22, 447–454.

Tuttle, M. P. (2005). New Madrid in motion. *Nature* 435, 1037–1039.

Vendeville, B. C., and Jackson, M. P. A. (1992). The fall of Diapirs during thin-skinned extension. *Mar. Petrol. Geol.* 9, 354–371. doi: 10.1016/0264-8172(92)90048-j

Welhan, J. A., and Lupton, J. E. (1987). Light-hydrocarbon gases in Guaymas basin hydrothermal fluids - thermogenic versus abiogenic origin. *AAPG Bull. -Am. Assoc. Petrol. Geol.* 71, 215–223.

White, J. D. L., and Ross, S. (2011). Maar-diatreme volcanoes: a review. *J. Volcanol. Geotherm. Res.* 201, 1–29. doi: 10.1016/j.jvolgeores.2011.01.010

Wyrick, D., Ferrill, D. A., Morris, A. P., Colton, S. L., and Sims, D. W. (2004). Distribution, morphology, and origins of Martian pit crater chains. *J. Geophys. Res. Planets* 109:E6.

Conflict of Interest: The authors declare that the research was conducted in the absence of any commercial or financial relationships that could be construed as a potential conflict of interest.